

**TMX2 is a crucial regulator of cellular redox state and its dysfunction causes severe brain developmental abnormalities.**

Laura V.Vandervore<sup>1,2,3\*</sup>, Rachel Schot<sup>1\*</sup>, Chiara Milanese<sup>4</sup>, Daphne J. Smits<sup>1</sup>, Esmee Kasteleijn<sup>1</sup>, Andrew E. Fry<sup>5,6</sup>, Daniela T. Pilz<sup>7</sup>, Stefanie Brock<sup>2,8</sup>, Esra Börklü-Yücel<sup>1,9,10</sup>, Marco Post<sup>9</sup>, Nadia Bahi-Buisson<sup>11</sup>, María José Sánchez-Soler<sup>12</sup>, Marjon van Slegtenhorst<sup>1</sup>, Boris Keren<sup>13</sup>, Alexandra Afenjar<sup>14</sup>, Stephanie A. Coury<sup>15</sup>, Wen-Hann Tan<sup>15,16</sup>, Renske Oegema<sup>17</sup>, Linda S. de Vries<sup>18</sup>, Katherine A. Fawcett<sup>19,20</sup>, Peter G.J. Nikkels<sup>21</sup>, Aida Bertoli-Avella<sup>22</sup>, Amal Al Hashem<sup>23</sup>, Abdulmalik A. Alwabel<sup>24</sup>, Kalthoum Tlili-Graïess<sup>25</sup>, Stephanie Efthymiou<sup>26</sup>, Faisal Zafar<sup>27</sup>, Nuzhat Rana<sup>27</sup>, Farah Bibi<sup>28</sup>, Henry Houlden<sup>26</sup>, Reza Maroofian<sup>26</sup>, Richard E. Person<sup>29</sup>, Amy Crunk<sup>29</sup>, Juliann M. Savatt<sup>30</sup>, Lisbeth Turner<sup>30</sup>, Mohammad Doosti<sup>31</sup>, Ehsan Ghayoor Karimiani<sup>32, 33</sup>, Nebal Waill Saadi<sup>34</sup>, Javad Akhondian<sup>35</sup>, Maarten H. Lequin<sup>36</sup>, Hülya Kayserili<sup>10</sup>, Peter J. van der Spek<sup>37</sup>, Anna C. Jansen<sup>2,38</sup>, Johan M. Kros<sup>39</sup>, Robert M. Verdijk<sup>39</sup>, Nataša Jovanov Milošević<sup>40</sup>, Maarten Fornerod<sup>9</sup>, Pier Giorgio Mastroberardino<sup>4,41</sup>, Grazia M. S. Mancini<sup>1\*\*</sup>

\*authors contributed equally

\*\* corresponding author: Grazia M.S. Mancini, Department of Clinical Genetics, Erasmus University Medical Center, 3000 CA Rotterdam, The Netherlands.

Email: [g.mancini@erasmusmc.nl](mailto:g.mancini@erasmusmc.nl)

**Author affiliations:**

<sup>1</sup>Department of Clinical Genetics, Erasmus University Medical Center (Erasmus MC), P.O. Box 2040, 3000 CA Rotterdam, The Netherlands

<sup>2</sup>Neurogenetics Research Group, Research Cluster Reproduction, Genetics and Regenerative Medicine, Vrije Universiteit Brussel, Brussels, 1090, Belgium

<sup>3</sup>Center for Medical Genetics, UZ Brussel, Brussels, 1090, Belgium

<sup>4</sup>Department of Molecular Genetics, Erasmus University Medical Center (Erasmus MC), P.O. Box 2040, 3000 CA Rotterdam, The Netherlands

<sup>5</sup>Institute of Medical Genetics, University Hospital of Wales, Cardiff CF14 4XW, UK

<sup>6</sup>Division of Cancer and Genetics, School of Medicine, Cardiff University, Cardiff CF14 4XN, UK

<sup>7</sup>West of Scotland Clinical Genetics Service, Queen Elizabeth University Hospital, Glasgow G51 4TF, UK

<sup>8</sup>Department of Pathology, UZ Brussels, Brussels, 1090, Belgium

<sup>9</sup>Department of Cell Biology, Erasmus University Medical Center (Erasmus MC), P.O. Box 2040, 3000 CA Rotterdam, The Netherlands

<sup>10</sup>Medical Genetics Department, Koç University School of Medicine (KUSoM), Istanbul, 34010, Turkey

<sup>11</sup>Imagine Institute, INSERM UMR-1163, Laboratory Genetics and Embryology of Congenital Malformations, Paris Descartes University, Institut des Maladies Génétiques 24, Boulevard de Montparnasse, Paris, 75015, France.

<sup>12</sup>Sección Genética Médica, Servicio de Pediatría, Hospital Clínico Universitario Virgen de la Arrixaca. IMIB-Arrixaca, Murcia, 30120, España.

<sup>13</sup>Département de génétique, Hôpital Pitié-Salpêtrière, Assistance Publique – Hôpitaux de Paris, Paris, 75013, France

<sup>14</sup>Département de génétique et embryologie médicale, CRMR des malformations et maladies congénitales du cervelet et des déficits intellectuels de causes rares, GRC ConCer-LD, Sorbonne Universités, Hôpital Trousseau, Paris, 75012, France.

<sup>15</sup>Division of Genetics and Genomics, Boston Children's Hospital, Boston, Massachusetts, 02115, USA

<sup>16</sup>Harvard Medical School, Boston, Massachusetts, 02115, USA

<sup>17</sup>Department of Genetics, University Medical Center Utrecht (UMCU), Utrecht University, 3584 CX, the Netherlands

<sup>18</sup>Department of Neonatology, University Medical Center Utrecht (UMCU), Utrecht University, 3584 CX, the Netherlands

<sup>19</sup>MRC Computational Genomics Analysis and Training Programme (CGAT), MRC Centre for Computational, Biology, MRC Weatherall Institute of Molecular Medicine, John Radcliffe Hospital, Headington, Oxford OX3 9DS, UK

<sup>20</sup>Present address: Department of Health Sciences, University of Leicester, George Davies Centre, University Road, Leicester LE1 7RH, UK

<sup>21</sup>Department of Pathology, University Medical Center Utrecht (UMCU), Utrecht University, 3584 CX, the Netherlands

<sup>22</sup>Centogene AG, Rostock, 18055, Germany

<sup>23</sup>Division of Medical Genetic, Department of Pediatrics, Prince Sultan Military Medical City, Riyadh, 12233, Saudi Arabia

<sup>24</sup>Division of General Pediatrics, Department of Pediatrics, Prince Sultan Military Medical City, Riyadh, 12233, Saudi Arabia

<sup>25</sup>Division of Neuroradiology, Department of Radiology, Prince Sultan Military Medical City, Riyadh, 12233, Saudi Arabia.

<sup>26</sup> Department of Neuromuscular Disorders, UCL Institute of Neurology, Queen Square, London WC1N 3BG, UK

<sup>27</sup>Department of Pediatric Neurology, Children's hospital and institute of Child health, Multan 60000, Pakistan

<sup>28</sup>University Institute of Biochemistry & Biotechnology, PMAS – Arid Agriculture University, Rawalpindi, 43600, Pakistan

<sup>29</sup>GeneDx, 207 Perry Parkway, Gaithersburg, MD, 20877, USA

<sup>30</sup>The Autism & Developmental Medicine Institute at Geisinger in Danville, PA 17822. USA

<sup>31</sup>Department of Molecular Genetics, Next Generation Genetic Polyclinic, Mashhad 009851, Iran

<sup>32</sup>Molecular and Clinical Sciences Institute, St. George's, University of London, Cranmer Terrace London, SW17 0RE, UK

<sup>33</sup>Innovative medical research center, Mashhad branch, Islamic Azad University, Mashhad 9133736351, Iran

<sup>34</sup>College of Medicine / Baghdad University, Children Welfare Teaching Hospital - Medical City Complex – Baghdad 10001, Iraq

<sup>35</sup>Department of Pediatric Neurology, Ghaem Hospital, Mashhad University of Medical Sciences, Mashhad 009851, Iran

<sup>36</sup>Department of Radiology, University Medical Center Utrecht (UMCU), Utrecht , 3584 CX, the Netherlands.

<sup>37</sup>Department of Pathology, Clinical Bio-informatics, Erasmus University Medical Center (Erasmus MC), P.O. Box 2040, 3000 CA Rotterdam, The Netherlands

<sup>38</sup>Pediatric Neurology Unit, Department of Pediatrics, UZ Brussel, Brussels, 1090, Belgium

<sup>39</sup> Department of Pathology, Erasmus University Medical Center (Erasmus MC), P.O. Box 2040, 3000 CA Rotterdam, The Netherlands

<sup>40</sup>Croatian Institute of Brain Research, School of Medicine, University of Zagreb, 10000, Croatia.

<sup>41</sup>Department of Life, Health and Environmental Sciences, University of L'Aquila, L'Aquila, 67100, Italy

Respective e-mail addresses: [Laura.Vandervore@vub.be](mailto:Laura.Vandervore@vub.be); [r.schot@erasmusmc.nl](mailto:r.schot@erasmusmc.nl); [c.milanese@erasmusmc.nl](mailto:c.milanese@erasmusmc.nl); [d.smits@erasmusmc.nl](mailto:d.smits@erasmusmc.nl); [e.kasteleijn@erasmusmc.nl](mailto:e.kasteleijn@erasmusmc.nl); [FryAE@cardiff.ac.uk](mailto:FryAE@cardiff.ac.uk); [PilzDT@cardiff.ac.uk](mailto:PilzDT@cardiff.ac.uk); [Stefanie.Brock@vub.be](mailto:Stefanie.Brock@vub.be); [eyucel@kuh.ku.edu.tr](mailto:eyucel@kuh.ku.edu.tr); [425194mp@student.eur.nl](mailto:425194mp@student.eur.nl); [nadia.bahi-buisson@nck.aphp.fr](mailto:nadia.bahi-buisson@nck.aphp.fr); [mj.sanchezsoler@gmail.com](mailto:mj.sanchezsoler@gmail.com); [m.vanslegtenhorst@erasmusmc.nl](mailto:m.vanslegtenhorst@erasmusmc.nl); [boris.keren@psl.aphp.fr](mailto:boris.keren@psl.aphp.fr); [alexandra.afenjar@aphp.fr](mailto:alexandra.afenjar@aphp.fr); [Stephanie.Coury@childrens.harvard.edu](mailto:Stephanie.Coury@childrens.harvard.edu); [Wen-Hann.Tan@childrens.harvard.edu](mailto:Wen-Hann.Tan@childrens.harvard.edu); [R.Oegema@umcutrecht.nl](mailto:R.Oegema@umcutrecht.nl); [L.s.devries@umcutrecht.nl](mailto:L.s.devries@umcutrecht.nl); [kath.a.fawcett@googlemail.com](mailto:kath.a.fawcett@googlemail.com); [P.G.J.Nikkels@umcutrecht.nl](mailto:P.G.J.Nikkels@umcutrecht.nl); [Aida.Bertoli-Avella@centogene.com](mailto:Aida.Bertoli-Avella@centogene.com); [amal.alhashem@gmail.com](mailto:amal.alhashem@gmail.com); [jrdr.alwabel@gmail.com](mailto:jrdr.alwabel@gmail.com); [Kalthoum.Tlili@rns.tn](mailto:Kalthoum.Tlili@rns.tn); [s.efthymiou@ucl.ac.uk](mailto:s.efthymiou@ucl.ac.uk); [drfaisal867@yahoo.com](mailto:drfaisal867@yahoo.com); [drnuzhatrana@gmail.com](mailto:drnuzhatrana@gmail.com); [h.houlden@ucl.ac.uk](mailto:h.houlden@ucl.ac.uk); [r.maroofian@ucl.ac.uk](mailto:r.maroofian@ucl.ac.uk); [rperson@genedx.com](mailto:rperson@genedx.com); [acrunk@genedx.com](mailto:acrunk@genedx.com); [jmsavatt@geisinger.edu](mailto:jmsavatt@geisinger.edu); [lturner3@geisinger.edu](mailto:lturner3@geisinger.edu); [doosti.m@gmail.com](mailto:doosti.m@gmail.com); [eghayoor@gmail.com](mailto:eghayoor@gmail.com); [nebalpedneu2013@gmail.com](mailto:nebalpedneu2013@gmail.com); [akhondianj@mums.ac.ir](mailto:akhondianj@mums.ac.ir) ;

[M.h.lequin@umcutrecht.nl](mailto:M.h.lequin@umcutrecht.nl);      [hkayserili@kuh.ku.edu.tr](mailto:hkayserili@kuh.ku.edu.tr);      [p.vanderspek@erasmusmc.nl](mailto:p.vanderspek@erasmusmc.nl);  
[Anna.Jansen@uzbrussel.be](mailto:Anna.Jansen@uzbrussel.be);      [j.m.kros@erasmusmc.nl](mailto:j.m.kros@erasmusmc.nl);      [r.verdijk@erasmusmc.nl](mailto:r.verdijk@erasmusmc.nl);  
[njovanov@gmail.com](mailto:njovanov@gmail.com);      [m.fornerod@erasmusmc.nl](mailto:m.fornerod@erasmusmc.nl);      [p.g.mastroberardino@erasmusmc.nl](mailto:p.g.mastroberardino@erasmusmc.nl);  
[g.mancini@erasmusmc.nl](mailto:g.mancini@erasmusmc.nl)

## ABSTRACT

The redox state of the neural progenitors regulates physiological processes such as neuronal differentiation, dendritic and axonal growth. The relevance of ER-associated oxidoreductases in these processes is largely unexplored. We describe a severe neurological disorder caused by biallelic loss of function variants in Thioredoxin (TRX)-Related Transmembrane-2 (*TMX2*), detected by exome sequencing in fourteen affected individuals from ten unrelated families presenting with congenital microcephaly, cortical polymicrogyria and other migration disorders. *TMX2* encodes one of the five TMX proteins of the Protein Disulfide Isomerase family, hitherto not linked to human developmental brain disease. Our mechanistic studies on protein function show that *TMX2* localizes to the ER Mitochondria-Associated-Membranes (MAMs), is involved in posttranslational modification and protein folding, and undergoes physical interaction with the MAM associated and ER folding chaperone calnexin and ER calcium pump SERCA2. These interactions are functionally relevant because *TMX2*-deficient fibroblasts show decreased mitochondrial respiratory reserve capacity and compensatory increased glycolytic activity. Intriguingly, under basal conditions *TMX2* occurs in both reduced and oxidized monomeric form, while it forms a stable dimer under treatment with hydrogen peroxide, recently recognized as signaling molecule in neural morphogenesis and axonal pathfinding. Exogenous expression of the pathogenic *TMX2* variants or of variants with *in vitro* mutagenized TRX domain induces a constitutive *TMX2* polymerization, mimicking increased oxidative state. Altogether these data uncover *TMX2* as a sensor in the MAM-regulated redox signaling pathway and identify it as a key adaptive regulator of neuronal proliferation, migration and organization in the developing brain.

## INTRODUCTION

The endoplasmic reticulum (ER) is responsible for the folding of one third of the human proteome. Protein folding is coordinated by ER chaperones, together with ER oxidoreductases of the Protein Disulfide Isomerase (PDI) family<sup>1</sup>. This family consists of 23 oxidoreductase proteins<sup>2</sup> and is part of the thioredoxin (TRX) superfamily<sup>3</sup>. PDIs are characterized by the presence of at least one TRX-like domain (potentially catalytically active with sequence including two cysteines, C-X-X-C) and an ER retention domain (typically Lys-Asp-Glu-Leu/ KDEL)<sup>3; 4</sup>. In the oxidizing environment of the ER, PDIs with active site cysteines can oxidize thiol groups of newly synthesized polypeptides mediating protein folding<sup>2; 5</sup>, but can also catalyze reduction and isomerization of disulfides in misfolded proteins, facilitating ER-associated degradation (ERAD) during the unfolded protein response (UPR)<sup>6</sup>.

PDI mediated protein folding is ATP dependent and relies on precise regulation of calcium influx to the mitochondria, necessary for mitochondrial oxidative phosphorylation<sup>1 7</sup>. Since the ER is the major storage site for calcium, specialized ion channels are located at the mitochondria-associated membranes (MAMs) of the ER to assure proper calcium transport to and from the ER, e.g. sarcoplasmic-endoplasmic reticulum Ca<sup>2+</sup>-ATPase ATP2A2/SERCA2, inositol 1,4,5 trisphosphate receptor type 1 (IP3R1) and voltage-dependent anion-selective channel 1 (VDAC1)<sup>1</sup>. Besides regulating protein folding, some PDI oxidoreductases additionally function in calcium trafficking through interaction with these ER calcium channels<sup>1; 8; 9</sup>. Accordingly, some PDIs show enriched ER localization at the MAM<sup>10</sup>. Through upregulation of calcium transport into the mitochondria, PDIs are also able to regulate ATP production, necessary to increase folding mechanisms when misfolded proteins aggregate (ER-stress)<sup>1; 7; 11</sup>. Hence, PDIs and protein folding are important determinants for normal mitochondrial bioenergetics and cell survival.

In humans, altered expression of PDIs has been correlated with neurodegenerative disorders like Alzheimer, Parkinson disease and amyotrophic lateral sclerosis<sup>12</sup>. However, notwithstanding their proven biological relevance, little is known about the consequence of inherited pathogenic variants in PDIs. At the moment of writing, only one heterozygous recurrent variant in *P4HB* (OMIM 176790) (Prolyl 4-hydroxylase,  $\beta$ -subunit) encoding PDIA1 has been associated with Cole-Carpenter syndrome 1 (OMIM 112240), characterized by skeletal malformations (OMIM 176790)<sup>12-15</sup>. Pathogenic variants in non-PDI oxidoreductases from other protein families, e.g. *WWOX* (OMIM 605131)<sup>16</sup>, *DHCR24* (OMIM 606418)<sup>17</sup>, *NDUFS1* (OMIM 157655)<sup>18</sup>, and variants in MAM-associated genes, e.g. *SERAC1* (OMIM 614725)<sup>19</sup>, *MFN2* (OMIM 608507)<sup>20</sup>, have been linked to neurodevelopmental and mitochondrial disorders.

Thioredoxin (TRX)-Related Transmembrane proteins (TMX) are five type 1 transmembrane proteins belonging to the PDI family<sup>2; 3; 21</sup>. The best studied of the group, TMX1 (PDIA11) is localized at the MAM and regulates calcium trafficking through interaction with the ER calcium pump SERCA2<sup>1 7</sup>. No pathogenic variants have been reported in TMX members in relation to human disease until now, although two missense variants of unknown significance in *TMX3* were proposed to lead to microphthalmia<sup>22</sup>. TMX2 (PDIA12), one of the least studied of the group, is encoded by *TMX2* on chromosome 11q12.1 (OMIM 616715), is ubiquitously expressed and presents in two isoforms, the longest with 296 amino acids being the most biologically relevant as ER resident protein<sup>21</sup>. The N-terminal signal sequence (amino acid1-48) is followed by the cytosolic domain (amino acid49-102), the single transmembrane domain (amino acid 103-125), the atypical TRX domain (amino acid 167-170, Ser-Asn-Asp-Cys, SNDC), the ER intraluminal C-terminal domain (amino acid 126-296) and a Di-

lysine ER retention motif (amino acid 293-296, Lys-Lys-Asp-Lys, KKDK)<sup>3; 4</sup>. It has been suggested that TMX2 is enriched at the MAM location<sup>10</sup>. Because TMX2 does not contain a typical thioredoxin-like active domain (SNDC instead of CXXC), its oxidoreductase activity and role in protein folding have been questioned. However, the importance of *TMX2* is underlined by the non-viability of homozygous *Tmx2*<sup>-/-</sup> knockout mice (C57BL/6NJ strain, Mouse Genome Informatics MGI:1914208). Here we report microcephaly, polymicrogyria (PMG), complex migration disorders and epilepsy in individuals bearing bi-allelic autosomal recessive variants in *TMX2*. We study the function of normal TMX2 and the effect of the variants in human cells providing a mechanistic understanding of TMX2 function in health and disease, linking PDIs to neurodevelopment.

## **MATERIAL AND METHODS**

### *Ethics statement and biopsy*

The cohort of *TMX2* affected individuals (here coded as P1 to P14) includes 10 families of which four were gathered through the European Network on Brain Malformations, Neuro-MIG (COST Action CA16118), five families through GeneMatcher<sup>23</sup> and one family was earlier described in supplemental data from a cohort of undiagnosed individuals with malformations of cortical development<sup>24</sup>. All study participants or their legal caretakers gave written informed consent to participate in this study and for publication of images, according to Erasmus MC institutional review board requirements (protocol METC-2012387). Skin biopsies were sampled before the study for routine diagnostic purposes and used to isolate dermal fibroblasts using standard procedures. Fibroblasts were tested negative for mycoplasma infection.

### *Neuropathology*

An autopsy including brain was performed after demise of individual P1 at 14 days of age and individual P10 at two days of age. The material was fixed in 4% formalin. Samples from frontal, parietal, temporal, and occipital lobes, deep nuclei, cerebellum, brain stem and spinal cord were submitted for histological evaluation. Paraffin-embedded samples were cut to a thickness of 5 µm and hematoxylin and eosin-staining (H&E) or Lugol-PAS staining were performed according to the manufacturer's guidelines (Hoffmann-LaRoche, Basel, Switzerland). For the age- and gender matched control brain, the sample collection was approved by the Institutional Ethical Review Board (EP02/21AG) of the Clinical Hospital Centre and School of Medicine, the University of Zagreb, in accordance with the Helsinki declaration 2000, and became a part of the Zagreb Neuroembryological Collection<sup>25</sup>.

### *Genomic and Transcriptomic analysis*

#### *Whole exome sequencing (WES)*

DNA was isolated from blood of the probands and family members and used for exome and Sanger sequencing, in nine different laboratories. WES data are deposited internally at the Erasmus MC and in each medical institute referring the individuals with *TMX2* variants, in respect to the privacy of the families. Details of sequencing and analysis pipelines are described in the **Supplemental data**.

#### *RNA sequencing*

Skin fibroblasts from affected individuals P1, P2 and four different healthy age and sex (male) matched controls were cultured to 80% confluence in T175 flasks, before RNA isolation with TRIzol™ Reagent (Invitrogen®, 15596026) and RNA cleanup with RNeasy mini kit (Qiagen®, 74106). The

NEBNext Ultra Directional RNA Library Prep Kit for Illumina was used to process the samples. Strand-specific mRNAseq libraries for the Illumina platform were generated with a poly-A selection and sequenced at GenomeScan (GenomeScan, Leiden, The Netherlands). Fastq files from forward and reverse reads were aligned to reference genome hg38 with the STAR aligner tool (v.2.4.2a)<sup>26</sup>. Counts per gene were calculated from bam files using the featureCount program with version 27 of the genecode hg38 annotation<sup>27</sup>. For differential gene expression P1 and P2's samples were compared to four male control samples in R (v.3.4.3) (R Core Team (2017). R: A language and environment for statistical computing. R Foundation for Statistical Computing, Vienna, Austria) using the edgeR package (v.3.20.9)<sup>28</sup>. Functional annotation clustering of the top 1000 differentially expressed genes ( $p < 0.05$ ) was performed with gene ontology Database for Annotation, Visualization and Integrated Discovery (DAVID, v6.8)<sup>29; 30</sup>. Downstream affected biological functions were determined with Ingenuity Pathway analysis (IPA, Qiagen®, vs.2018) on all differentially expressed genes with a p-value below 0.05.

#### *qPCR*

Skin fibroblasts were cultured in T75 culture flasks, in DMEM with 10% Fetal Calf Serum (FCS), 1% PenStrep, Lonza® (DMEM with serum), to 80% confluence. Total RNA was extracted on RNeasy mini columns (Qiagen®, 74106) according to the manufacturer's protocol. Reverse transcription was performed on 1 µg of RNA in a total volume of 20 µl, with the iScript cDNA Synthesis kit (Bio-Rad Laboratories®) used according to the manufacturer's instructions. Real time quantitative Polymerase Chain Reaction (RT-qPCR) was performed using iTaq™ Universal SYBR® Green Supermix (BioRad®) according to manufacturer's instructions. Primers for RT-qPCR analysis for the experiments shown in Fig. 3 are listed in Table S1.

#### *Antibodies*

Primary antibodies used: Polyclonal Rabbit anti-human TMX2 (HPA040282, Sigma®, WB 1:250), Monoclonal Rabbit anti-human HSP60 (D6F1, Cell Signaling®, Immunocytochemistry (ICC) dilution 1:800), Monoclonal Rabbit anti-human CNX (C5C9, Cell Signaling®, ICC 1:50, IP 1:1000), Mouse monoclonal anti-SERCA2 ATPase (ab2861, Abcam IP:1:1000), Mouse monoclonal anti-Myc (9B11, Cell Signaling Technologies®, WB 1:3000 and ICC 1:500), Mouse monoclonal anti-PDI (1D3, ADI-SPA-891, Enzo Life Sciences, WB: 1:1000)

Secondary antibodies used for ICC: Green Goat anti-Rabbit IgG (H+L) Alexa Fluor 488 (1:400, Thermo Fisher Scientific®, A11088), Red Cy™3 AffiniPure Donkey Anti-Mouse IgG (H+L) (1:100, Jackson Laboratories®, 715-165-150). Secondary antibodies used for WB in 1 in 10 000: Red IRDye® 680RD Goat anti-Rabbit IgG (H + L) (LI-COR Biosciences®, 926-68071), Green IRDye® 800CW Goat anti-Mouse IgG (H + L) (LI-COR Biosciences®, 926-32210).

#### *Plasmid constructs*

Wild-type human *TMX2* (NM\_015959) was cloned in a pCMV-Entry-Myc-DDK TrueORF Gold vector (OriGene®, RC200032). 50 µL semi-competent homemade *Escherichia coli* XL10-Gold Bacteria strains were thawed on ice for 20 minutes and subsequently incubated for 15 minutes with 0.1 µg wild-type *TMX2* plasmid. Transformation of the bacterial cells was induced through a heat shock at 42°C for 2 minutes. 800 µL Luria-Bertani (LB) broth (EZ™ Mix, Lennox®) was added to the cells and placed under agitation (200 rpm, 40 min, 37°C). Selection of transformed cells was performed overnight on LB-Kanamycin agar plates at 37°C. Vector-positive colonies were grown to 50 mL midprep. Plasmid DNA



was isolated with the Qiagen® Plasmid Plus Midi kit. The full length and sequence of *TMX2* cDNA in the plasmid was checked by capillary sequencing before performing the transfections. pcDNA™3.1/Myc-His (-)/LacZ (Thermo Fisher Scientific®) was used as a negative control and kindly provided by Dr. Mark Nellist.

#### *Site-directed Mutagenesis (SDM)*

Variant *TMX2* constructs (TRX domain SNDC to SNDG p.Cys170Gly and affected individuals' variants p.Arg53Cys and p.Arg231Trp) were generated according to manufacturers' procedures using the QuikChange II XL Site-Directed Mutagenesis Kit (Agilent®), wild-type purified *TMX2* construct dilution (10 ng/μL) and 100 ng/μL primers specified in Table S2. PCR products were transformed in ultracompetent *Escherichia coli* XL10-Gold bacteria supplemented with β-mercaptoethanol in SOC medium through a heat shock at 42°C for 30 seconds. Selection, midi isolation and Sanger sequencing were performed in analogy with the wild-type construct.

#### *Sanger sequencing of plasmid DNA*

Sanger sequencing of wild-type and variant plasmid DNA was performed as earlier described<sup>31</sup>. Briefly, amplification reactions were performed in a total volume of 20 μL, containing 1× PCR buffer with Mg (Roche), 200 μM of each dNTP, 1 μM forward and reverse primer (specified in Table S3), 0.1 units Fast Start Taq DNA polymerase (Roche), and 25 ng genomic DNA. PCR conditions were as follows: 5' 96°C, 10 cycles of 30" 96°C, 30" 68°C (-1°C/cycle), 60" 72°C, followed by 25 cycles of 30" 96°C, 30" 58°C, 60" 72°C, and a final extension for 5' 72°C.

PCR reactions were purified with ExoSAP-IT (USB). Direct sequencing of both strands was performed with Big Dye Terminator chemistry (version 3.1; Applied Biosystems). DNA fragment analysis was performed with capillary electrophoresis on an ABI 3130 Genetic Analyzer (Applied Biosystems) with the software package Seqscape (Applied Biosystems, version 2.1).

#### *Transfection*

Human Embryonic Kidney HEK293T cells were plated at  $5 \times 10^4$  cells/cm<sup>2</sup> with or without 24 mm cover slips (Thermo Fisher Scientific®) cultured in 2mL DMEM with serum in a 6 well plate or 10 cm petri dishes for immunoprecipitation. The next day culture media was replaced with 2 mL DMEM without serum (Lonza®). Per 10 cm<sup>2</sup>, 1 μg plasmid DNA was added to 125 μL DMEM without serum at room temperature and 3 μL/10cm<sup>2</sup> Lipofectamine™ 2000 Transfection Reagent (Thermo Fisher Scientific®) was added to 125 μL DMEM without serum. These tubes mixed and incubated 5 minutes at room temperature, prior to transfection. The appropriate volume was added to each dish in a dropwise manner. After 3 hours, 10% FCS and 1% PenStrep was supplemented to the dishes. After 24h transfection, cells were fixated with methanol for 10 minutes at -20°C or lysed for western blot and immunoprecipitation. Transfection was also stable after 48 and 72h (Fig.S3).

#### *Immunoprecipitation (IP) and Mass spectrometry (MS)*

Exogenous *TMX2* was immunoprecipitated after transfection in HEK293T cells. Initially, 15 μL EZview Red Anti-c-Myc Affinity Gel beads (E6654, Sigma Aldrich®) were washed with non-denaturing TNE-1% lysis buffer (50mM Tris pH 7.6 + 100mM NaCl + 50mM NaF + 1% NP-40 + 1mM EDTA + Protease inhibitor tab Roche®). *TMX2*-transfected and control Lac-Myc-transfected HEK293T cells in 10 cm Petri's dishes were transferred on ice, washed with 1×dPBS, and lysed with 800 μL TNE-1% lysis buffer. To test transfection efficiency and localization, each dish contained a 24 mm coverslip, which

was subsequently fixated and immunostained, before adding the lysis buffer. Lysates were incubated on ice for 10 minutes and centrifuged at 10000 x g for 10 minutes at 4°C. The supernatant was added to the washed beads and incubated overnight under agitation at 4°C. After washing 3 times with TNE-1% lysis buffer and centrifugation at 1000 x g, 15 sec, 4°C, bead pellets were subjected to a Mass spectrometry preparation as described<sup>32</sup>. Protein Mascot scores and numbers of unique peptides were taken directly from the Mascot output and reported. Only hits with a Mascot score higher than 40 were taken into account for analysis.

#### *Mitochondrial respiration and glycolysis determination*

Bioenergetics profiles of human primary skin fibroblasts were generated in real time with a Seahorse XF24 Extracellular Flux Analyzer (Agilent Technologies, Santa Clara, Ca, USA) as previously described<sup>33</sup>. Fibroblasts were seeded on a Seahorse XF-24 plate at a density of  $6 \times 10^4$  cells per well and grown overnight in DMEM with serum at 37 °C, 5% CO<sub>2</sub>. This density ensures a proportional response to the uncoupler FCCP (Carbonyl cyanide 4-(trifluoromethoxy)phenylhydrazone) with cell number and resulted in confluent cultures, in which cell replication was further prevented by contact inhibition. On the experimental day, medium was changed to unbuffered DMEM (XF Assay Medium – Agilent Technologies, Santa Clara, Ca, USA) supplemented with 5 mM glucose and 1 mM sodium pyruvate, and incubated 1 hour at 37 °C in the absence of CO<sub>2</sub>. Medium and reagent acidity was adjusted to pH 7.4 on the day of the assay, according to manufacturer's procedure. Mitochondrial respiration was measured as the oxygen consumption rate (OCR), and glycolysis was measured as the extracellular acidification rate (ECAR). After three baseline measurements for the oxygen consumption ratio (OCR), cells were sequentially challenged with injections of mitochondrial toxins: 0.5 μM oligomycin (ATP synthase inhibitor), 1 μM FCCP (mitochondrial respiration uncoupler), 0.5 μM rotenone (complex I inhibitor), and 0.5 μM antimycin (complex III inhibitor).

For galactose experiments, cells were cultured in galactose 10 mM, 10% FCS, 2 mM glutamine, 5 mM HEPES and 1% penicillin-streptomycin medium for three days before the bioenergetics assay<sup>33</sup>.

A minimum of two Seahorse replicates were performed for each fibroblast line. In each replicate, we used six wells for each line. In each run, six wells were always used for a reference primary fibroblast line with highly characterized bioenergetics behavior. Three reference lines that were available at the Erasmus MC institute have been used<sup>33</sup>.

Basal respiration was defined as the average OCR values at baseline. Respiration dedicated to ATP production was calculated as difference between basal respiration and the respiration measured after oligomycin injection. Reserve capacity was calculated as the difference between the maximal respiration (the average OCR of the three measurements following the FCCP injection) and basal respiration. The rotenone dependent respiration parameter was calculated as the difference between the maximal respiration value and the average OCR values obtained after the rotenone injection and was used to evaluate the activity of mitochondrial complex I. Basal glycolysis was defined as the average of the 3 baseline ECAR measurements, and the increase in glycolysis after blocking ATP synthase was indicated as oligomycin stimulated glycolysis.

#### *TMX2 Redox state assay*

HEK293T cells were transfected during 24 hours with plasmid DNA producing Myc-tagged β-lactamase control protein (Lac-Myc), wild-type (TMX2) or variant TMX2 (p.Cys170Gly, p.Arg53Cys and p.Arg231Trp) in a 6 well plate. Afterwards cells were treated with different ER-stress inducers or oxidant/reductant at 37°C with 5% CO<sub>2</sub>, according to Matsuo et al <sup>34</sup>: 6h with 0,5 μg/mL Brefeldin A

(BFA; Cayman Chemical® CAS 20350-15-6, 20 mg/mL stock in DMSO), 6h with 5 µM Thapsigargin (TG, Sigma® T9033, 1mM stock in DMSO), 6h with 10 µg/mL Tunicamycin (TM, Sigma® T7765, 1mg/mL stock in DMSO), 10 minutes with 5 mM DL-Dithiothreitol (DTT, Fluka® CAS 3483-12-3, 100 mM stock in MilliQ sterile water), or 10 minutes with 200 µM Hydrogen peroxide H<sub>2</sub>O<sub>2</sub> (Merck®, 822287). Free thiol groups were alkylated by washing and 10 min incubating the cells with ice-cold 1× dPBS (Sigma Aldrich®) supplemented with 20 mM N-ethylmaleimide (NEM, Sigma®, E3876-5G) and 4× Laemmli buffer (3:1) before storage at -20°C. Total protein concentrations were determined by a BCA protocol with Varioskan™ LUX multimode microplate reader (Thermo Fisher Scientific®). Equal protein concentrations were loaded onto a 4-15% Criterion™ TGX Stain-Free™ Protein Gel (Bio-Rad Laboratories®). Proteins were separated in a non-reducing SDS-PAGE with a Criterion™ Cell geltank (Bio-Rad Laboratories®) at 100 Volt for 1h40min in Tris-Glycine-SDS running buffer. Proteins were transferred by wet blotting to a Nitrocellulose membrane (Amersham Protran 0.45 NC, GE Healthcare Life Sciences®) at 100 Volt for 1h at 4°C or alternatively on a Trans-Blot Turbo 0.2 µm Nitrocellulose membrane (BioRad®) at 25V, 1.5A for 20 minutes in a Trans-Blot Turbo transfer system (BioRad®). After antibody incubation, bands were detected with a fluorescent based approach on the Odyssey Infrared Imager (LI-COR Biosciences®). Densitometry analysis to determine Dimer/monomer ratios was performed in Odyssey 3.0 Software or Image Studio Lite Version 5.2.

### Statistics

Statistical tests were performed with GraphPad 8 and are specified in legends of the experiments.

## RESULTS

### Clinical overview

The clinical features observed in all fourteen individuals, in whom we detected *TMX2* variants, have been summarized in **Table 1** and full clinical and MRI description is available in the Supplemental Note, **Table S4** and **Figure 1**. Most subjects (11/14) were reported with microcephaly (defined as OFC at or below -2.5 SD, for age and sex; **Table 1**) and, where documented, this was present at birth or at the first clinical examination. However, intra-familial discrepancy is present, because only one of the two siblings of family 5 was microcephalic at adult age (P5), while the other sibling has a borderline normal head circumference (P4) in the third decade of life. Two other affected individuals of family 9 and 10 did not present with microcephaly at the last examination (**Table 1**, P13 and P14). With the exclusion of two individuals (P6 and P14), all have suffered from drug-resistant epilepsy, occurring in most cases in early infancy, characterized by apnea, epileptic spasms, myoclonic seizures, focal seizures with or without secondary generalization, generalized tonic clonic (GTC) seizures and in one case possible diaphragmatic myoclonia. Three affected individuals of the cohort died during infancy, two of them of severe epilepsy in the early post-natal period. The brain imaging of these two is strikingly similar (**Figure 1**, P1 and P10) and resembles a congenital viral (CMV) infection for the presence, besides diffuse bilateral polymicrogyria (PMG), of reduced central white matter volume, abnormal appearance of the periventricular borders with an occipital pseudocyst. In both cases no infection was documented, and brain pathology excluded the presence of inflammatory signs. All subjects, but one (Family 10, P14) surviving beyond infancy present with severe developmental delay (**Table 1**), progressing to profound intellectual disability, cerebral palsy with absent ambulation and lack of speech and/or progressive neurodegenerative course. No additional extra-CNS malformations or health issues were observed, except for expected complications of the underlying brain pathology. Metabolic screening performed in most subjects

did not reveal abnormalities of intermediate or energy metabolism. Two individuals have been followed in their third decade (P4 and P5): they both showed signs of regression, with loss of motor skills and severely impaired cognitive skills and no speech development.

Structural brain abnormalities were detected in almost all the subjects undergoing MRI scan. In seven of the twelve affected individuals who received an MRI scan (**Figure 1**) a cortical malformation has been documented. Diffuse PMG (small and excessive number of gyri) was observed in five individuals (**Figure 1**, P1, P2, P3, P10 and P12), while the two siblings from family 5 show diffuse pachygyric (= thickened and smooth) cortex (**Figure 1**, P6-P7). The brain imaging of these latter siblings had been reported in supplemental data from a cohort of undiagnosed individuals with malformations of cortical development<sup>24</sup>. In three other individuals brain imaging shows (progressive) global cerebral atrophy (families 4 and 6). The two remaining affected individuals showed an MRI with no cortical malformation (P14) or a hemihypertrophy with frontal dysgyria (P13). No brain imaging was performed in individual P8 (Family 6) and individual P11 (Family 8).

### **Brain pathology of affected individuals (P1 and P10)**

At autopsy of individual P1 (day 14 postpartum), the head circumference was 34 cm (-2SD) and the brain weight 316 g (normal weight at term: 400-450 g). Macroscopically, the brain surface was polymicrogyric with the temporal regions being least affected (**Figure 2A and 2B**).

Evaluation of H&E stained sections of the frontal, parietal, temporal and occipital cortex showed extensive unlayered polymicrogyria throughout the sampled cortical sections (**Figure 2E and 2F**). Undulating bands of neurons extended deeply in the cortex. The insular and parahippocampal region were least affected with undulating neuronal bands extending less deep into the cortex. The hippocampus was spared. The transition from normal cortex to polymicrogyric cortex was abrupt. The molecular layer appeared fused between adjacent gyri causing inclusions of pial vessels in the deep cortical region. Leptomeninges overlying the polymicrogyric cortex were focally thickened. Overmigration of neurons into the arachnoid space was not noted. The grey-white matter junction was blurred under affected cortical areas. The white matter was normal. Heterotopic remnants of the germinal matrix were occasionally observed in the periventricular region which is considered pathologic given that the affected individual was born at term. Telangiectatic vessels were present in the brain stem at the level of the locus coeruleus. Histologically, other brain structures and the eyes, especially the retina appeared normal. There were no signs of mitochondrial disease or an acquired cause for the malformation, e.g. no calcifications or inflammatory cells. The basal ganglia were normal as well as the cerebellum, which consisted of a four-layered cortex including the for the age appropriate external granular layer.

Brain examination of individual P10 (**Figure 2C**) macroscopically showed a polymicrogyric cortex of the occipital lobes, but microscopically the whole cerebral cortex was polymicrogyric, with diffuse dyslamination, fusion of molecular layers and blurred grey-white matter junction (**Figure 2G**). In contrast with P1, in the polymicrogyric areas glioneuronal heterotopia were diffusely seen migrating over the meninges in P10's brain. In the frontal area few calcifications were seen at the grey-white matter border, with some calcification of the pericallosal artery, without any other evidence for (focal) infection or inflammation. The occipital ependymal layer showed interruptions and gliotic changes with some reactive macrophages. The presence of neuroglial cells migrating over the glia limitans of the pia into the arachnoid space is typical of the cobblestone malformation. However,

there were no additional abnormalities common in the cobblestone malformation, such as brainstem and cerebellar hypoplasia<sup>35</sup>.

### Genomic and Transcriptomic analysis

Biallelic variants in *TMX2* were identified in fourteen affected individuals from ten unrelated pedigrees by whole exome sequencing (WES), compatible with autosomal recessive inheritance. Detailed information on the genomic alterations (cDNA alteration, protein alteration, gnomAD frequency, SIFT, MutationTaster and CADD scores) are described in **Table S4** and **Supplemental Results** and a schematic overview of the gene and the thirteen discovered variants can be found in **Figure 3A**. *TMX2* encodes a transcript of 8 exons (NM\_015959.3), which is translated into a protein with 296 amino acids. To test the effect of each variant on *TMX2* mRNA expression transcriptomic analysis was performed. RT-qPCR in skin fibroblasts from the affected newborn **P1** of **Family 1** with a compound heterozygous mutation in *TMX2* (c.164A>C, p.Asp55Ala; c.391dup, p.Leu131Profs\*6), showed that *TMX2* mRNA expression was much lower (nearly half fold), compared to healthy controls (**Figure 3 B**). To determine which of the alleles was still expressed, we performed allele specific RT-qPCR (primers specified in **Table S1**). Results showed that the allele carrying the frameshift in exon 4 barely expressed any product (2-3% of total level *TMX2* mRNA in healthy controls), indicating that very likely the transcript is subjected to nonsense mediated decay (NMD) (**Figure 3C**). When amplifying the other allele, total *TMX2* mRNA expression was again reduced to approximately half, confirming our previous result (**Figure 3B**) and showing that the allele with the c.164A>C, p.Asp55Ala variant is normally expressed (**Figure 3C**).

In **Family 2**, the proband (**P2**) had a homozygous *TMX2* missense change in the ultimate nucleotide of exon 6 (c.614G>A, p.Arg205Gln), with a predicted effect on splicing. RT-qPCR did not show significant decrease in expression of *TMX2* mRNA in skin fibroblasts from the proband, compared to healthy controls (**Figure 3B**). However, since the variant affected the last nucleotide of an exon, an effect on mRNA splicing was suspected. We used RNAseq in combination with Integrated Genomics Viewer (IGV) to visualize cumulative transcript reads per exon in a Sashimi plot (**Figure 3D**) and the amount of reads per million were calculated (**Figure 3E**). The c.614G>A, p.Arg205Gln variant indeed affected splicing through introduction of a new internal splice site in exon 6, resulting into four different transcripts: regular mRNA, an alternative transcript with a loss of 11 nucleotides within exon 6, an alternative transcript with full in-frame exon 6 skipping (loss of 66 nucleotides) and mRNA with intron 6 retention (**Figure 3E**). This latter transcript is also present at low level in healthy controls. Individual reads of each transcript are shown in **Figure S1**.

In **Family 3**, individual P3, similar to the variants in individual P1, a combination was found of a missense change in exon 1 (c.157C>T, p.Arg53Cys, nearby the p.Asp55Ala of P1, together with a nonsense variant leading to a premature stop codon in the last exon of *TMX2* (c.757C>T, p.Arg253\*). The effect of the variants on *TMX2* transcription in skin fibroblasts was tested. RT-qPCR showed a mean decreased level of *TMX2* mRNA expression by 23%, potentially indicating that the premature termination codon in the last exon of the transcript partially escapes nonsense mediated decay, as being less than 50 to 55 nucleotides from the stop codon at the 3'-end (for *TMX2* nt836-891) (**Figure 3B**)<sup>36</sup>.

For families 4 to 10 no materials were available to test the transcriptional effect of each variant. However, considering lethality in *Tmx2* null mice, residual *TMX2* transcript can be anticipated originating from the missense alleles and/ or the allele creating a new splice acceptor site (P10).

### **Gene ontology (GO) analysis of differentially expressed genes in *TMX2* pathogenic variants**

Our data clearly indicates that biallelic *TMX2* variants lead to reduced *TMX2* expression, acting as loss of function variants (LoF) (**Figure 3**). Compared to other TMX family members, only *TMX2* is expressed steadily from week 8 throughout fetal brain development, even increasing during postnatal life (mRNA expression during human brain development retrieved from Allen human brain atlas **Figure S3**). We therefore considered the *TMX2* variants as probably explanatory for the early neurological manifestation and decided to investigate their effect in detail.

We performed analysis of RNAseq data from cultured skin fibroblasts of two affected individuals (P1 and P2), in parallel with three age and gender matched controls, and studied which pathways were deregulated.

#### *Functional annotation clustering analysis*

Functional annotation clustering analysis of the top 1000 significant differentially expressed genes (DEGs) ( $p < 0.05$ ), by the Database for Annotation, Visualization and Integrated Discovery (DAVID, v6.8) ranked the top cluster of genes as those associated with post-translational modifications, i.e. intramolecular or intermolecular disulfide bond formation (Annotation Cluster 1: Disulfide bond  $p = 9.9 \times 10^{-24}$ ) and N-linked glycosylation (Annotation Cluster 1: Glycoprotein  $p = 2.1 \times 10^{-28}$  and Glycosylation site:N-linked  $p = 2.5 \times 10^{-27}$ ) (**Figure 4A**). From this cluster of genes, 24 disulfide containing genes were subtracted as being the highest deregulated of this cluster in cells from affected individuals, having a False Discovery Rate (FDR) lower than 0.05 (**Figure 4B**). Stringent filtering (FDR < 0.01) without clustering, uncovered 37 differentially expressed genes of which five were indirectly controlled by the UPR or regulate expression of UPR markers, i.e. *CXCL5* (OMIM 600324)<sup>37</sup>, *DAPK1* (OMIM 600831)<sup>38</sup>, *HGF* (OMIM 142409)<sup>39</sup>, *LTBP1* (OMIM 150390)<sup>40</sup> and *CES1* (OMIM 114835)<sup>41</sup>. Interestingly, the second highest deregulated gene *LTBP1* encodes a known folding substrate for another PDI protein, ERp46, also known as TXNDC5<sup>42; 43</sup>. Although it has been suggested that most PDIs show substrate specificity<sup>2</sup>, *LTBP1* could also be a substrate of *TMX2* or *TMX2* might affect TXNDC5 mediated folding.

The second most significant functional annotation cluster ranks genes having a transmembrane domain (Enrichment score= 9.43) and a third most significant cluster contains genes encoding proteins involved in synaptic function, specifically located at the postsynaptic membrane (Enrichment Score= 4.63). This latter membrane is enriched with receptors and ion channels, essential for the interaction with neurotransmitters. Interestingly, another cluster mentions the deregulation of calcium ion binding (Annotation Cluster 6 Enrichment score 3.16).

#### *Ingenuity pathway analysis (IPA)*

Ingenuity pathway analysis (IPA) of the same differentially expressed genes in cells from the two probands ( $p < 0.05$ ), taking into account the logarithmic Fold Change (LogFC) of each gene, was used to calculate the most affected biological functions and diseases networks (**Figure 4C**). Only activation Z-scores in the 90 percent confidence interval were considered to be significant ( $Z[-\infty, -1.65]$  and  $Z[1.65, +\infty]$ ). Interestingly, this analysis showed two key IPA categories being inhibited in *TMX2* affected individuals, i.e. 'Nervous System Development and Function' and 'Cellular Growth, Proliferation and Survival' (Blue bars in **Figure 4C**). The most significant inhibited function was

'quantity of neurons' (Z=-2.864), with a decreased outgrowth of cells (Z= -2.818), specifically neurons (Z=-2.594) and neurites (Z= -2.46), all related to processes affected in microcephaly. Consequently, transcripts related to learning ability (Z= -2.356) and cognition function (Z= -2.257) were also shown to be potentially decreased in cells from affected individuals. Moreover, besides the development of neurons (Z= -1.955), the differentiation of neurons was highly inhibited (Z= -1.812). Lastly, overall cell survival (Z= -1.785) and viability (Z= -2.016) were decreased. When looking at the most activated biological functions or associated diseases, seizures (Z=2.712) and seizure disorder (Z=2.819) are the most significant activated features (Red bars in **Figure 4C**).

### **Proteomics analysis of exogenous TMX2**

In view of the effect of *TMX2* variants on transcriptome, specifically on disulfide bond formation, we wondered whether *TMX2* functions as an oxidoreductase and/or chaperone in protein folding. A transfection protocol was optimized in HEK293T cells with a Myc-tagged vector containing full length *TMX2* sequence (p.CMV6.TMX2-Myc/DKK) and a Myc-tagged  $\beta$ -lactamase vector as negative control (pcDNA<sup>TM</sup>3.1/Myc-His (-)/LacZ). Immunocytochemistry of exogenous *TMX2* localized the protein to the MAM through co-localization with the marker Calnexin (CNX) (**Figure S4 A**) and in the vicinity of the mitochondria, visualized by mitochondrial marker HSP60 (**Figure S4 B**). Next, we aimed at the identification of the *TMX2* interacting proteins, by performing mass spectrometry-based proteomics of co-precipitated proteins. A 24-hour over-expression of Myc-tagged *TMX2*, followed by immunoprecipitation and LC-MS/MS reveals 71 unique peptides as putative interactors. The list of reproducible co-precipitated proteins is shown in **Table S5** and visualized with Cytoscape String App according to pathway involvement in **Figure 5A**. A first interesting observation was that *TMX2* physically interacts with MAM marker CNX, which is a calcium-binding protein folding chaperone. Other PDIs have also been shown to bind with CNX, e.g. *TMX1*<sup>2</sup>, *TMX4*<sup>6</sup>, ERp57<sup>2</sup>. Binding was reciprocally confirmed after IP of CNX and detection of Myc-tagged *TMX2* on western blots (**Figure 5B**). Besides CNX, multiple other protein folding regulators and ER chaperones were interacting with *TMX2* (**Figure 5, dark blue**), i.e. co-chaperones of the HSP70 family DNAJA2(HSP40) and BCL2 associated athanogene 2(BAG2), chaperonin containing TCP1 subunit 5 (CCT5), Translocon-associated protein/TRAP subunit alpha (SSR1), N-glycosylation regulators glucosidase II alpha subunit (GANAB) and Dolichyl-diphospho-oligosaccharide-protein glycosyltransferase complex (OST complex: RPN2, DDOST, STT3B, MLEC)<sup>44</sup>.

Furthermore, besides CNX, *TMX2* bound with other key-regulators of calcium homeostasis, i.e.  $\text{Ca}^{2+}$ -binding proteins (RCN2, HAX1, SSR1) and  $\text{Ca}^{2+}$ -ion channels located at the MAM or mitochondrial membrane (ATP2A2/SERCA2, VDAC1) (**Figure 5A, light blue**). *TMX2* also binds to Erlin-2 which directly regulates inositol 1,4,5-trisphosphate  $\text{Ca}^{2+}$  receptor degradation. These calcium receptors and channels are necessary for mitochondrial bioenergetics. SERCA2, like CNX, is a main interactor of some PDI members (*TMX1*<sup>7</sup>, ERdj5<sup>1</sup>) and described as a key regulator of protein folding. Binding was confirmed reciprocally after immunoprecipitation of SERCA2 and detection of Myc-tagged *TMX2* on western blot (**Figure 5B**). Proteomics data also indicates physical interaction of *TMX2* with components of mitochondrial outer and inner membrane complexes (**Figure 5A, green**), e.g. the mitochondrial contact site and cristae organizing system (MICOS, MIC60/IMMT subunit), the mitochondrial precursor protein import pathways (TOM22 and TIM23 complex)<sup>45</sup>, and the mitochondrial membrane respiratory chain NADH dehydrogenase (Complex I NDUFA2 and NDUFA12 subunits).

TMX2 also interacted with proteins regulating the unfolded protein response, i.e. DDRGK1, a direct regulator of IRE1 $\alpha$ -XBP1 and PERK-eIF2 $\alpha$ -CHOP signaling<sup>46</sup>, or the UPR associated endoplasmic reticulum-associated degradation (ERAD), dependent on an ubiquitin-proteasome system (UPS) (**Figure 5, red**), i.e. TMX2 binds with VCP-AMFR ERAD complex, Erlin-2 involved in ERAD of IP3Rs, Ubiquitin-binding protein UBXN1, deubiquitinating enzyme USP25, and proteasome subunits PSMD2, PSMD3 and PSMA5. Because of these interactions, the RNAseq showing dysregulated genes indirectly linked to UPR signaling and the role of TMX2 in protein folding, we tested the hypothesis whether *TMX2* variants activated the UPR, specifically the IRE1 $\alpha$ -XBP1 and PERK-eIF2 $\alpha$ -CHOP signaling. RT-qPCR of UPR downstream mRNA markers *CHOP* and spliced *XBP1* was performed for the three available fibroblasts lines derived from affected individuals and showed that aberrant TMX2 did not affect the amount of expressed *sXPB1*, nor *CHOP* (**data not shown**). Although the RNAseq data of affected individuals showed DEGs indirectly linked to the UPR, no direct factors of any of the three UPR pathways were found to be upregulated when *TMX2* was mutated. Hence, together these data indicate that *TMX2* pathogenic variants do not lead to constitutive UPR activation in fibroblasts from affected individuals.

### **Mitochondrial bioenergetics in *TMX2* variant fibroblasts**

PDIs and protein folding are important determinants for normal mitochondrial bioenergetics and cell survival. In view of the putative function of TMX2 at the ER-MAM-mitochondria interface, the results of RNAseq (hinting towards a deregulated disulfide bond formation and calcium binding in cells from affected individuals) and proteomics analysis (showing binding with regulators of protein folding, ERAD, ER-mitochondrial UPR and Calcium homeostasis), we focused on mitochondrial activity and evaluated mitochondrial respiration and glycolytic activity in *TMX2* variant fibroblasts derived from three affected individuals (P1, P2 and P3) using a Seahorse Extracellular Flux Analyzer. Only P3 showed reduced basal mitochondrial activity and reduced respiration dedicated to ATP production when compared to healthy control lines. At the same time, all *TMX2* variant fibroblasts featured suppressed mitochondrial respiration upon stimulation with the mitochondrial uncoupler FCCP, with a significantly reduced reserve capacity – which reflects the bioenergetics reservoir available to counteract cellular stress - and overall decreased rotenone dependent respiration. The latter indicates a reduced activity of mitochondrial complex I (**Figure 6A and 6C**). Interestingly, P1 and P2, but not P3 showed a significant increase in the glycolytic activity – that was measured as lactate dehydrogenase mediated acidification of the medium- both in basal condition and upon stimulation with the mitochondrial ATP-synthase inhibitor oligomycin (**Figure 6B and 6D**), indicating that *TMX2* variant fibroblasts compensated the mitochondrial bioenergetics defects by potentiating the glycolytic pathway and glucose catabolism. Quantification of cellular ATP levels showed no differences between *TMX2* affected individuals and controls (**Figure S5**). To identify potential mitochondrial defects silenced in glycolysis permitting conditions, we performed the experiments also in conditions where glycolysis was inhibited by the presence of galactose, forcing cells to rely on mitochondrial respiration for ATP production. As expected, P1 and P2 failed to potentiate basal respiration and showed no significant increase of respiration dedicated to ATP production and of mitochondrial complex I activity when cultured in galactose medium, although retained the ability to potentiate the reserve capacity (**Figure 6E**).

### **Redox state analysis of wild-type and variant *TMX2***

*TMX2 oxidizes and reduces in native conditions*



We tested whether thiol groups in TMX2 can be oxidized and reduced and thus whether TMX2 is able to form disulfides, hence would be able to influence protein folding. HEK293T cells were transiently transfected with *TMX2* (**Figure 7A**) or  $\beta$ -lactamase vector (**Figure 7B**) and the redox state of TMX2 was monitored before and after treatment with the reducing agent DTT, the oxidant hydrogen peroxide ( $H_2O_2$ ) or the ER-stress inducers: Brefeldin A (ER-Golgi transport blocker) (**Figure 7 A-B**), Thapsigargin (SERCA2 inhibitor) or Tunicamycin (N-glycosylation inhibitor) (**Figure 7C**). To be able to distinguish redox state of cysteines, cells were incubated with a cysteine alkylating reagent N-ethylmaleimide (NEM) to covalently bind reduced thiol groups (+0.125kDa /thiol), but not oxidized disulfide groups. **Figure 7A**, lane 1 and 5, shows that TMX2 exists in both a reduced NEM alkylated form (~33 kDa) and an oxidized lower molecular form (~31 kDa) in native conditions. These two bands were consistently found in all of our repeat experiments with the ratios of oxidized and reduced TMX2 alternating, e.g. sometimes more reduced TMX2 (**Figure 7A, lane 1**), sometimes equal amount (**Figure 7C, lane 1**), and sometimes more oxidized TMX2. ER stress induced by BFA, tunicamycin or thapsigargin did not alter TMX2 redox state (**Figure 7A, lane 2, 6 and Figure 7C lane 2, 5, 6**) nor its' protein level. DTT treatment partially shifted redox state to a more reduced TMX2 (**Figure 7A, lane 3**) and TMX2 was completely reduced in the presence of  $\beta$ -mercaptoethanol (**Figure 5B and S6**), indicating that at least part of TMX2 redox state is thiol mediated.

#### *TMX2 dimerizes and oxidative stress elevates dimer/monomer ratio*

Surprisingly,  $H_2O_2$ -mediated oxidation of cells overexpressing TMX2 did not result in an increase of the lower oxidized TMX2 band, as we observed for PDI (PDIA1) (**Figure 7A, lane 12**), but generated an intense TMX2-reactive extra band with higher molecular mass on immunoblot (**Figure 7A, lane 4 and 8**; apparent mass ~65kDa). Since molecular mass was double the amount of a TMX2 monomer, we hypothesize that this band represents a slower migrating homodimer. Dimer/monomer ratios were calculated, showing up to a 200 fold increase of dimerization in oxidative environment (**Figure 7D**,  $H_2O_2$   $p=0.0005$ ). The dimer was still present when SDS-PAGE was performed in reducing conditions with  $\beta$ -mercaptoethanol and without NEM, although the ratio dimer/monomer was almost inverted and the monomer represented the major band (**Figure S6**). These results indicated that oxidative conditions mediated by  $H_2O_2$ , induce dimerization of TMX2 and that this dimerization is at least partially mediated by disulfide bond formation. Homodimerization was confirmed through linear correlation between the observed molecular weight on blot (average 57.8kDa,  $n=18$ ) and the calculated expected molecular weight with the method of Lambin for a gradient SDS-PAGE gel (4-15%) (**Figure S7**)<sup>47</sup>.

#### *TMX2 variants highly dimerize and polymerize in native and ER-stress conditions*

We tested the effect of variants on the behavior of exogenously expressed TMX2. By in vitro mutagenesis, the single cysteine in the atypical thioredoxin domain was substituted with a glycine, p.Cys170Gly. Interestingly, ablation of the active cysteine in the TRX domain still permitted dimerization, which supports the hypothesis that this dimer is not a mixed disulfide dimer of the TRX domain with another substrate. Moreover, dimerization of TMX2 was appreciated in the TRX domain variant, even under native conditions, i.e. independently of an oxidative stress, suggesting that this domain is involved in the reversibility of the TMX2 state between monomer and dimer (**Figure 7E**). Furthermore, oxidative stress even induced the formation of higher molecular weight polymers in the TRX domain mutant (**Figure 7C, lane 10**). To determine redox state of human *TMX2* pathogenic variants under different stress conditions, we overexpressed either a *TMX2* variant located in the

cytosolic domain, p.Arg53Cys, or a variant in the ER lumen domain, p.Arg231Trp (**Figure 7C, lanes 13-18, 19-24**). Strikingly, the amount of TMX2 dimer was significantly higher compared to wild-type TMX2 for both variants in both native and under all stress conditions, not only H<sub>2</sub>O<sub>2</sub>, as quantified in **Figure 7E**. Dimer/ monomer ratios were increased by 10-fold (1:1), while in wild-type TMX2 this is 0.1:1, showing that the pathogenic variants block the protein in a dimerized state and that affected individuals may have less monomeric protein available (**Figure 7E**). Moreover, TMX2 with the natural variants also displayed higher levels of polymerization, as seen in the TRX mutant (apparent mass ~110kDa and 140kDa, observed average mass 97.1kDa and 138.9kDa with method of Lambin in n=11). Based on the linear correlation between observed and expected mass, these bands seem to represent homotrimers and tetramers of TMX2 (**Figure S7**). Although the amount of dimer to monomer ratios under oxidative stress was also doubled or tripled in mutant p.Arg231Trp or p.Arg53Cys TMX2 compared to wild-type TMX2, the difference was no longer significant (**Figure 7E, H<sub>2</sub>O<sub>2</sub>, fourth graph**). DTT treatment prevented polymerization of the variants almost completely, confirming that polymerization is (at least partially) mediated by disulfide bridge formation (**Figure 7E, third graph and Figure S6**). Notably, in vitro mutagenized Myc-tagged TMX2 was still able to bind both CNX and SERCA2 (**Figure S8**).

## DISCUSSION

We describe a disorder, characterized by developmental delay, microcephaly, impaired speech and ambulation, epilepsy and cortical malformations, with a relatively wide spectrum of severity ranging from early death to intellectual disability with mild motor impairment, resulting from recessive *TMX2* variants.

Redox regulatory proteins are enriched at the MAM of the smooth ER<sup>10; 48</sup>. Some of these proteins interact with ER calcium handling proteins and regulate the calcium flux into the mitochondria, which, in turn, influences mitochondrial membrane potential and mitochondrial respiration<sup>1</sup>. Thioredoxins of the PDI family regulate the cellular redox state through oxidoreductase activity-mediated disulfide bond formation and contribute to protein folding. The PDI transmembrane ER thioredoxin-related (TMX) proteins, such as MAM-associated TMX1, seem to have dual function: on the one hand in regulating protein folding, maintaining the redox environment of the ER and hereby preventing ER stress, on the other hand in regulating calcium flux in the mitochondria<sup>7</sup>. Besides regulating protein folding and calcium transport, thioredoxins in general are key molecules in the regulation of oxidative stress through scavenging reactive oxygen species (ROS), such as hydrogen peroxide<sup>49</sup>.

TMX2 lacks the canonical oxidoreductase active C-X-X-C domain. However, its function as folding chaperone is suggested by our data, demonstrating (1) the dysregulation of disulfide bond and N-glycosylation-related genes in *TMX2*-deficient fibroblasts, (2) the interaction of TMX2 with several proteins regulating protein folding and UPR and (3) the presence of both oxidized and reduced forms in the maleimide alkylation assay. In addition, our mechanistic studies discover the function of TMX2 as regulator of calcium homeostasis and mitochondrial bioenergetics. TMX2 localizes at the MAM where it physically binds to calnexin and SERCA2, whereas *TMX2*-variant fibroblasts show decreased mitochondrial reserve capacity and lower ability to cope with oxidative stress, probably related to defective calcium flux, similarly to what was proposed for *TMX1*-deficient cells<sup>7</sup>. Compared to *TMX1*, *TMX2* is highly expressed in fetal and post-natal brain. The specific *TMX2* expression in the cortex during prenatal life, together with the deleterious effect of its loss of function for human cortical development, places TMX2 as a key molecule in the ER-mitochondrial redox regulation of brain

development. Although pathogenic variants in mitochondrial oxidoreductases and MAM-associated proteins have been reported as causes of pediatric neurologic disorders<sup>16-20</sup>, the TMX2 related disorder is a malformation of cortical development resulting from a defect in a member of the PDI family.

TMX2 is thus an important regulator of oxidative stimuli and an intriguing aspect is its responsiveness to H<sub>2</sub>O<sub>2</sub>. The sensitivity of TMX proteins to H<sub>2</sub>O<sub>2</sub> has received little attention, although it has been shown that their redox state dramatically changes after H<sub>2</sub>O<sub>2</sub>-treatment, as it happens for example for TMX4<sup>6</sup>. The hydrogen peroxide signaling molecule has long been considered as deleterious for cellular function and as a byproduct of oxidoreductase reactions, being rapidly metabolized by catalases, glutathione-peroxidases or peroxi-redoxins<sup>49</sup>. However, more recent findings highlighted the role of H<sub>2</sub>O<sub>2</sub> as physiological regulator of redox signaling (oxidative eustress), acting via reversible cysteine and methionine oxidation<sup>50</sup>. Additionally, H<sub>2</sub>O<sub>2</sub> functions in higher concentrations as a mediator of pathophysiological signals (oxidative distress) leading to growth arrest and regulated cell death<sup>50</sup>. One of the main intracellular sites of H<sub>2</sub>O<sub>2</sub> production is the ER<sup>51</sup>. Along with the activation of peroxi-redoxins as possible intermediate sensors, the role of H<sub>2</sub>O<sub>2</sub> in the development of the nervous system has been well-established<sup>51-53</sup>. Among targets of H<sub>2</sub>O<sub>2</sub> redox signaling are transcription factors of the Wnt and the Shh pathways<sup>54</sup>. Moreover, H<sub>2</sub>O<sub>2</sub> has been recently discovered as signaling molecule controlling axonal path finding in zebra fish<sup>54</sup> and neuronal growth cone collapse in vitro<sup>55</sup>. Hence, it is not surprising that a *TMX2* variant-mediated imbalance in oxidative eustress/distress could result in impaired neuronal development.

Under our experimental conditions, increased concentrations of H<sub>2</sub>O<sub>2</sub> in the culture medium induced wild-type TMX2 dimerization. In the same maleimide alkylation assays, TMX2 redox state does not seem sensitive to ER stressors. These results reflect a physiological sensitivity of TMX2 to H<sub>2</sub>O<sub>2</sub>, possibly mimicking an adaptive response to oxidative eustress, regulating physiological steps in development<sup>52; 54</sup>. Wild-type TMX2 dimer was still slightly present under β-mercaptoethanol reducing conditions (Fig. S6), indicating that it is partially formed through inter-disulfide bonds. The occurrence of homo-dimerization of other members of the PDI superfamily has been described earlier (for PDI<sup>56-58</sup>, PDIp<sup>59</sup>, ERp29<sup>60</sup>) and is suggested as a general mechanism to regulate PDI function<sup>13; 56</sup>. Dimers can exhibit higher chaperone or unfolding activity as described for ERp29, PDIp, CNX and CRT dimerization<sup>60</sup>. Also, homo-dimerization of other TMX proteins has been postulated, e.g. a putative TMX1 homodimer was observed in immunoprecipitates with anti-CNX after ablation of the TRX domain active cysteines<sup>61</sup>.

Our data suggest the formation of TMX2 homo-dimer/polymers, based on the evidence that observed TMX2 molecular masses on gradient gels show linearity with the predicted molecular mass by the Lambin method calculation and on the fact that the dimerization is not strictly dependent on disulfide bridge formation. Both under DTT pre-treatment in culture (of the TMX2 mutants) and by running a gel with β-mercaptoethanol, dimers are still present with an identical linear molecular mass. Since dimerization still occurs in the TRX domain mutant independently of an active cysteine and H<sub>2</sub>O<sub>2</sub> treatment, the dimer does not represent a heterodimer of TMX2 with a substrate formed through mixed disulfides, similar to what is described for TMX1 homo-dimerization<sup>61</sup>. Although polymers were also observed after ablation of the TRX domain cysteine, they were barely present under reducing conditions. Hence, we cannot exclude interactions of TMX2 with other substrates of identical molecular mass, through TRX domain-independent interactions. For example, N-linked glycosylation has been shown to modulate the formation of PDI polymers and in TMX2 it could mediate interaction with heterologous peptides<sup>56</sup>.

Similar to wild-type TMX2 under oxidative stress, we observed constitutive TMX2 homodi-/polymerization upon expression of the *TMX2* pathogenic variants (p.Arg53Cys and p.Arg231Trp), leading to mitochondrial dysfunction, reduced maximal respiration and increased glycolysis, as seen under ER stress conditions<sup>7; 50; 62</sup>. However, we did not detect activation of UPR in fibroblasts from affected individuals, both under native and under treatment with H<sub>2</sub>O<sub>2</sub> (data not shown). This suggests that UPR is not the primary target of TMX2 function or that cultured fibroblasts are not the ideal test model.

Another fascinating aspect is TMX2 involvement in the pathogenesis of PMG. This malformation has long been considered as a defect of postmigratory cortical organization<sup>63</sup>, with wide genetic heterogeneity, but also being a proven consequence of prenatal brain injury or disruptive events<sup>64</sup>. These aspects make genetic counseling of PMG most challenging. At brain imaging it may be difficult to distinguish PMG resulting from environmental factors (e.g. prenatal CMV infection) or from genetic defects. At MRI and pathological examination the main PMG characteristics are many small gyri with pebbled appearance, loss of normal cortical lamination, overfolding and fusion of the gyri, stippling of the white-grey matter border<sup>65</sup>, sometimes giving the appearance of generally thickened cortex. The cobblestone malformation is characterized by pebbled cerebral surface, thick cortex and striation perpendicular to the cortical surface, which reflect tracks of neuroglial cells overmigrating above the glia limitans in the subarachnoid space, overmigration sometimes being massive and leading to thinning of the cortical plate<sup>35; 66</sup>. Cobblestone malformation is frequently associated with cerebellar and pons dysplasia and variable hydrocephalus, white matter and callosal dysgenesis. PMG and cobblestone malformation have been sporadically reported to coexist in the same genetic disorder<sup>67; 68</sup>. Pathology of the brain in two *TMX2* variant affected individuals shows a complete disorganization of the cortical layers (unlayered PMG) in both and in one of them (P10) diffusely overmigrating neurons, typical of cobblestone malformation, together with scattered white matter calcifications and pseudocysts, suggestive of a disruptive (CMV-like) event. Unlayered PMG is supposed to be caused by an early disruption of cortical development between 16-24 weeks gestation<sup>69</sup> and can also be observed in metabolic causes of PMG such as Zellweger disease (a peroxisomal biogenesis disorder, characterized by mislocalization of catalase), or lining non-genetic schizencephalic clefts<sup>64; 70</sup>. A mixture of disruptive and developmental migratory abnormalities has been reported for the brain disorder caused by the Zika virus (ZIKV) infection, where the effect on neuronal proliferation and migration is more prominent than in other more common congenital infections, i.e. CMV<sup>71</sup>. We demonstrate that *TMX2*-related PMG is a disorder of neuronal migration and cortical organization, without evidence of vascular or inflammatory disruption, in some cases with radiological aspect resembling an infectious i.e. non-genetic cause, in other cases microscopically showing the cobblestone malformation. These observations support the view that PMG and cobblestone are cortical malformations that can share a common pathogenesis and represent different severity of the spectrum<sup>72; 73</sup>.

It is possible that some of the *TMX2* related malformations are caused by lack of physiological response to regulators of neuronal development (hypothetically H<sub>2</sub>O<sub>2</sub>-mediated axonal pathfinding) and some are the effect of abnormal oxidoreductase-mediated protein folding and calcium homeostasis, with a secondary mitochondrial dysfunction. Although no UPR stimulation was found in *TMX2* deficient cells, *TMX2* also plays a role in regulation of UPR and apoptosis, both mechanisms essential for regulation of neuronal proliferation and cortical organization<sup>74</sup>.

Our observation shows how in humans a genetic disorder of cellular redox adaptation mechanisms can be the cause of neuronal proliferation and migration disorders, with characteristics of a disruptive event. These studies also provide a mechanistic explanation for the fact that human brain development is driven by steps strictly regulated in time and space, including individual response to environmental stimuli, e.g. to redox signaling molecules and changes in cellular redox state. Protein disulfide isomerase family members might prove to be major players in this process.

#### **SUPPLEMENTAL DATA**

Supplemental data include 8 figures and 5 tables.

#### **DECLARATION OF INTERESTS**

The authors declare no competing interests.

#### **ACKNOWLEDGMENTS**

We thank the families for participating in this study. This publication is in part a result of collaboration within the European Network on Brain Malformations funded by COST (European Cooperation in Science and Technology, Action CA16118). We thank Dr. Mark Nellist for sharing materials for IP experiments, Dr. Jeroen A.A. Demmers and Dick H.W. Dekkers of the Proteomics Center core facility, Erasmus University Medical Center for help with mass spectrometry, Dr. Frans W. Verheijen for critically reading the manuscript and prof. Dr Robert Hofstra for continuous support. We thank the Erasmus MC Cancer Computational Biology Center for giving access to their IT infrastructure and the software that was used for various computations and data analyses in this study.

#### **FUNDING**

LVV was supported by Steunfonds Marguerite-Marie Delacroix, Research Foundation Flanders (FWO travel grant V429317N) and COST Action CA16118 (STSM grant #39032). SB is supported by the COST Action CA16118 (STSM grant # 576). EBY is supported by the COST Action CA16118 (STSM grant # 39362). AF, DTP, NBB, RO, MHL, HK, ACJ, NJM, GMSM are members of the European Network on Brain Malformations, Neuro-MIG (COST Action CA16118). A.E.F. and D.T.P. were supported by the Newlife Foundation for Disabled Children (Grant Reference: 11-12/04), Wales Epilepsy Research Network, and Wales Gene Park. ACJ is supported by a Senior Clinical Investigator Fellowship from the Research Foundation Flanders (FWO). GMSM is supported by the ZonMW TOP grant #91217045 and by private donations. Data from families 8,9 and 10 were collected as part of the SYNAPS Study Group collaboration funded by The Wellcome Trust and strategic award (Synaptopathies) funding (WT093205 MA and WT104033AIA). This research was conducted as part of the Queen Square Genomics group at University College London, supported by the National Institute for Health Research University College London Hospitals Biomedical Research Centre. The studies were funded by MRC (MR/S01165X/1, MR/S005021/1, G0601943), The National Institute for Health Research University College London Hospitals Biomedical Research Centre, Rosetree Trust, Ataxia UK, MSA Trust, Brain Research UK, Sparks GOSH Charity, Muscular Dystrophy UK (MDUK), Muscular Dystrophy Association (MDA USA).

#### **WEB RESOURCES**

Allen Brain Atlas <http://human.brain-map.org/>

BWA <http://bio-bwa.sourceforge.net/>  
DAVID <https://david.ncifcrf.gov/>  
dbSNP <https://www.ncbi.nlm.nih.gov/SNP/>  
ESP <http://evs.gs.washington.edu/EVS/>  
ExAc database <http://exac.broadinstitute.org>  
GeneMatcher <http://www.genematcher.org>  
Genome Analysis Toolkit <http://www.broadinstitute.org/gatk/>  
gnomAD database <http://gnomad.broadinstitute.org>  
Ingenuity <https://www.qiagen.com/us/shop/analytics-software/biological-data-tools/ingenuity-pathway-analysis/#orderinginformation>  
Mouse Genome Informatics <http://www.informatics.jax.org/>  
OMIM <https://www.omim.org/>  
R <https://www.R-project.org/>

#### **DATA AVAILABILITY AND ACCESSION NUMBERS**

WES data are deposited internally at the Erasmus MC and in each medical institute referring the affected individuals, in respect to the privacy of the families. The mass spectrometry proteomics data have been deposited in the ProteomeXchange Consortium<sup>75</sup> via the PRIDE<sup>76</sup> partner repository with the dataset identifier PXD014064. The accession number for the RNAseq data reported in this paper is Gene Expression Omnibus GSE133483.

#### **REFERENCES**

1. Gutiérrez, T., and Simmen, T. (2018). Endoplasmic reticulum chaperones tweak the mitochondrial calcium rheostat to control metabolism and cell death. *Cell Calcium* 70, 64-75.
2. Pisoni, G.B., Ruddock, L.W., Bulleid, N., and Molinari, M. (2015). Division of labor among oxidoreductases: TMX1 preferentially acts on transmembrane polypeptides. *Molecular Biology of the Cell* 26, 3390-3400.
3. Galligan, J.J., and Petersen, D.R. (2012). The human protein disulfide isomerase gene family. *Hum Genomics* 6, 6.
4. Ellgaard, L., and Ruddock, L.W. (2005). The human protein disulphide isomerase family: substrate interactions and functional properties. *EMBO Rep* 6, 28-32.
5. Okumura, M., Kadokura, H., and Inaba, K. (2015). Structures and functions of protein disulfide isomerase family members involved in proteostasis in the endoplasmic reticulum. *Free Radical Biology and Medicine* 83, 314-322.
6. Sugiura, Y., Araki, K., Iemura, S., Natsume, T., Hoseki, J., and Nagata, K. (2010). Novel thioredoxin-related transmembrane protein TMX4 has reductase activity. *J Biol Chem* 285, 7135-7142.
7. Raturi, A., Gutierrez, T., Ortiz-Sandoval, C., Ruangkittisakul, A., Herrera-Cruz, M.S., Rockley, J.P., Gesson, K., Ourdev, D., Lou, P.H., Lucchinetti, E., et al. (2016). TMX1 determines cancer cell metabolism as a thiol-based modulator of ER-mitochondria Ca<sup>2+</sup> flux. *J Cell Biol* 214, 433-444.

8. Halperin, L., Jung, J., and Michalak, M. (2014). The many functions of the endoplasmic reticulum chaperones and folding enzymes. *IUBMB Life* 66, 318-326.
9. Carreras-Sureda, A., Pihán, P., and Hetz, C. (2018). Calcium signaling at the endoplasmic reticulum: fine-tuning stress responses. *Cell Calcium* 70, 24-31.
10. Lynes, E.M., Bui, M., Yap, M.C., Benson, M.D., Schneider, B., Ellgaard, L., Berthiaume, L.G., and Simmen, T. (2012). Palmitoylated TMX and calnexin target to the mitochondria-associated membrane. *Embo j* 31, 457-470.
11. Vance, J.E. (2014). MAM (mitochondria-associated membranes) in mammalian cells: lipids and beyond. *Biochim Biophys Acta* 1841, 595-609.
12. Andreu, C.I., Woehlbier, U., Torres, M., and Hetz, C. (2012). Protein disulfide isomerases in neurodegeneration: From disease mechanisms to biomedical applications. *FEBS Letters* 586, 2826-2834.
13. Parakh, S., and Atkin, J.D. (2015). Novel roles for protein disulphide isomerase in disease states: a double edged sword? *Frontiers in Cell and Developmental Biology* 3, 30.
14. Perri, E.R., Thomas, C.J., Parakh, S., Spencer, D.M., and Atkin, J.D. (2015). The Unfolded Protein Response and the Role of Protein Disulfide Isomerase in Neurodegeneration. *Front Cell Dev Biol* 3, 80.
15. Rauch, F., Fahiminiya, S., Majewski, J., Carrot-Zhang, J., Boudko, S., Glorieux, F., Mort, J.S., Bachinger, H.P., and Moffatt, P. (2015). Cole-Carpenter syndrome is caused by a heterozygous missense mutation in P4HB. *Am J Hum Genet* 96, 425-431.
16. Abdel-Salam, G., Thoenes, M., Afifi, H.H., Körber, F., Swan, D., and Bolz, H.J. (2014). The supposed tumor suppressor gene WWOX is mutated in an early lethal microcephaly syndrome with epilepsy, growth retardation and retinal degeneration. *Orphanet journal of rare diseases* 9, 12-12.
17. Zolotushko, J., Flusser, H., Markus, B., Shelef, I., Langer, Y., Heverin, M., Björkhem, I., Sivan, S., and Birk, O.S. (2011). The desmosterolosis phenotype: spasticity, microcephaly and micrognathia with agenesis of corpus callosum and loss of white matter. *European journal of human genetics : EJHG* 19, 942-946.
18. Hoefs, S.J., Skjeldal, O.H., Rodenburg, R.J., Nedregaard, B., van Kaauwen, E.P., Spiekerkotter, U., von Kleist-Retzow, J.C., Smeitink, J.A., Nijtmans, L.G., and van den Heuvel, L.P. (2010). Novel mutations in the NDUFS1 gene cause low residual activities in human complex I deficiencies. *Mol Genet Metab* 100, 251-256.
19. Wortmann, S.B., Vaz, F.M., Gardeitchik, T., Vissers, L.E.L.M., Renkema, G.H., Schuurs-Hoeijmakers, J.H.M., Kulik, W., Lammens, M., Christin, C., Kluijtmans, L.A.J., et al. (2012). Mutations in the phospholipid remodeling gene SERAC1 impair mitochondrial function and intracellular cholesterol trafficking and cause dystonia and deafness. *Nature Genetics* 44, 797.
20. Larrea, D., Pera, M., Gonnelli, A., Quintana-Cabrera, R., Akman, H.O., Guardia-Laguarta, C., Velasco, K.R., Area-Gomez, E., Dal Bello, F., De Stefani, D., et al. (2019). MFN2 mutations in Charcot-Marie-Tooth disease alter mitochondria-associated ER membrane function but do not impair bioenergetics. *Human Molecular Genetics* 28, 1782-1800.

21. Meng, X., Zhang, C., Chen, J., Peng, S., Cao, Y., Ying, K., Xie, Y., and Mao, Y. (2003). Cloning and identification of a novel cDNA coding thioredoxin-related transmembrane protein 2. *Biochem Genet* 41, 99-106.
22. Chao, R., Nevin, L., Agarwal, P., Riemer, J., Bai, X., Delaney, A., Akana, M., JimenezLopez, N., Bardakjian, T., Schneider, A., et al. (2010). A male with unilateral microphthalmia reveals a role for TMX3 in eye development. *PLoS one* 5, e10565-e10565.
23. Sobreira, N., Schiettecatte, F., Valle, D., and Hamosh, A. (2015). GeneMatcher: a matching tool for connecting investigators with an interest in the same gene. *Hum Mutat* 36, 928-930.
24. Zillhardt, J.L., Poirier, K., Broix, L., Lebrun, N., Elmorjani, A., Martinovic, J., Saillour, Y., Muraca, G., Nectoux, J., Bessieres, B., et al. (2016). Mosaic parental germline mutations causing recurrent forms of malformations of cortical development. *Eur J Hum Genet* 24, 611-614.
25. Judas, M., Simic, G., Petanjek, Z., Jovanov-Milosevic, N., Pletikos, M., Vasung, L., Vuksic, M., and Kostovic, I. (2011). The Zagreb Collection of human brains: a unique, versatile, but underexploited resource for the neuroscience community. *Ann N Y Acad Sci* 1225 Suppl 1, E105-130.
26. Dobin, A., Davis, C.A., Schlesinger, F., Drenkow, J., Zaleski, C., Jha, S., Batut, P., Chaisson, M., and Gingeras, T.R. (2013). STAR: ultrafast universal RNA-seq aligner. *Bioinformatics* 29, 15-21.
27. Liao, Y., Smyth, G.K., and Shi, W. (2014). featureCounts: an efficient general purpose program for assigning sequence reads to genomic features. *Bioinformatics* 30, 923-930.
28. Robinson, M.D., McCarthy, D.J., and Smyth, G.K. (2010). edgeR: a Bioconductor package for differential expression analysis of digital gene expression data. *Bioinformatics* 26, 139-140.
29. Huang da, W., Sherman, B.T., and Lempicki, R.A. (2009). Systematic and integrative analysis of large gene lists using DAVID bioinformatics resources. *Nat Protoc* 4, 44-57.
30. Huang da, W., Sherman, B.T., and Lempicki, R.A. (2009). Bioinformatics enrichment tools: paths toward the comprehensive functional analysis of large gene lists. *Nucleic Acids Res* 37, 1-13.
31. Oegema, R., Baillat, D., Schot, R., van Unen, L.M., Brooks, A., Kia, S.K., Hoogeboom, A.J.M., Xia, Z., Li, W., Cesaroni, M., et al. (2017). Human mutations in integrator complex subunits link transcriptome integrity to brain development. *PLoS Genet* 13, e1006809.
32. Vandervore, L.V., Schot, R., Kasteleijn, E., Oegema, R., Stouffs, K., Gheldof, A., Grochowska, M.M., van der Sterre, M.L.T., van Unen, L.M.A., Wilke, M., et al. (2019). Heterogeneous clinical phenotypes and cerebral malformations reflected by rotatin cellular dynamics. *Brain : a journal of neurology* 142, 867-884.
33. Milanese, C., Payán-Gómez, C., Galvani, M., Molano González, N., Tresini, M., Nait Abdellah, S., van Roon-Mom, W.M.C., Figini, S., Marinus, J., van Hilten, J.J., et al. (2019). Peripheral mitochondrial function correlates with clinical severity in idiopathic Parkinson's disease. *Movement Disorders*.
34. Matsuo, Y., and Hirota, K. (2017). Transmembrane thioredoxin-related protein TMX1 is reversibly oxidized in response to protein accumulation in the endoplasmic reticulum. *FEBS Open Bio* 7, 1768-1777.



35. Devisme, L., Bouchet, C., Gonzalès, M., Alanio, E., Bazin, A., Bessières, B., Bigi, N., Blanchet, P., Bonneau, D., Bonnières, M., et al. (2012). Cobblestone lissencephaly: neuropathological subtypes and correlations with genes of dystroglycanopathies. *Brain* 135, 469-482.
36. Zhang, Z., Xin, D., Wang, P., Zhou, L., Hu, L., Kong, X., and Hurst, L.D. (2009). Noisy splicing, more than expression regulation, explains why some exons are subject to nonsense-mediated mRNA decay. *BMC biology* 7, 23-23.
37. Zou, W., Bai, Y., Wang, X., Cheng, K., Sun, H., Zhang, G., and Yang, Z. (2017). PERK-Phosphorylated eIF2alpha Pathway Suppresses Tumor Metastasis Through Downregulating Expression of Programmed Death Ligand 1 and CXCL5 in Triple-Negative Breast Cancer. *Cancer Biother Radiopharm* 32, 282-287.
38. Gade, P., Ramachandran, G., Maachani, U.B., Rizzo, M.A., Okada, T., Prywes, R., Cross, A.S., Mori, K., and Kalvakolanu, D.V. (2012). An IFN-gamma-stimulated ATF6-C/EBP-beta-signaling pathway critical for the expression of Death Associated Protein Kinase 1 and induction of autophagy. *Proc Natl Acad Sci U S A* 109, 10316-10321.
39. Nita, I., Hostettler, K., Tamo, L., Medova, M., Bombaci, G., Zhong, J., Allam, R., Zimmer, Y., Roth, M., Geiser, T., et al. (2017). Hepatocyte growth factor secreted by bone marrow stem cell reduce ER stress and improves repair in alveolar epithelial II cells. *Sci Rep* 7, 41901.
40. Wolters, P.J., Collard, H.R., and Jones, K.D. (2014). Pathogenesis of idiopathic pulmonary fibrosis. *Annual review of pathology* 9, 157-179.
41. Wu, R., Zhang, Q.-H., Lu, Y.-J., Ren, K., and Yi, G.-H. (2015). Involvement of the IRE1 $\alpha$ -XBP1 pathway and XBP1s-dependent transcriptional reprogramming in metabolic diseases. *DNA and cell biology* 34, 6-18.
42. Jessop, C.E., Watkins, R.H., Simmons, J.J., Tasab, M., and Bulleid, N.J. (2009). Protein disulphide isomerase family members show distinct substrate specificity: P5 is targeted to BiP client proteins. *J Cell Sci* 122, 4287-4295.
43. Horna-Terrón, E., Pradilla-Dieste, A., Sánchez-de-Diego, C., and Osada, J. (2014). TXNDC5, a newly discovered disulfide isomerase with a key role in cell physiology and pathology. *International journal of molecular sciences* 15, 23501-23518.
44. Lakkaraju, A.K., Abrami, L., Lemmin, T., Blaskovic, S., Kunz, B., Kihara, A., Dal Peraro, M., and van der Goot, F.G. (2012). Palmitoylated calnexin is a key component of the ribosome-translocon complex. *The EMBO journal* 31, 1823-1835.
45. Harbauer, A.B., Zahedi, R.P., Sickmann, A., Pfanner, N., and Meisinger, C. (2014). The protein import machinery of mitochondria-a regulatory hub in metabolism, stress, and disease. *Cell Metab* 19, 357-372.
46. Liu, J., Wang, Y., Song, L., Zeng, L., Yi, W., Liu, T., Chen, H., Wang, M., Ju, Z., and Cong, Y.-S. (2017). A critical role of DDRGK1 in endoplasmic reticulum homeostasis via regulation of IRE1 $\alpha$  stability. *Nature Communications* 8, 14186.
47. Lambin, P. (1978). Reliability of molecular weight determination of proteins by polyacrylamide gradient gel electrophoresis in the presence of sodium dodecyl sulfate. *Analytical Biochemistry* 85, 114-125.

48. Gilady, S.Y., Bui, M., Lynes, E.M., Benson, M.D., Watts, R., Vance, J.E., and Simmen, T. (2010). Ero1alpha requires oxidizing and normoxic conditions to localize to the mitochondria-associated membrane (MAM). *Cell Stress Chaperones* 15, 619-629.
49. Yoshihara, E., Chen, Z., Matsuo, Y., Masutani, H., and Yodoi, J. (2010). Thiol redox transitions by thioredoxin and thioredoxin-binding protein-2 in cell signaling. *Methods Enzymol* 474, 67-82.
50. Sies, H. (2017). Hydrogen peroxide as a central redox signaling molecule in physiological oxidative stress: Oxidative eustress. *Redox Biol* 11, 613-619.
51. Winterbourn, C.C. (2017). Biological Production, Detection, and Fate of Hydrogen Peroxide. *Antioxidants & Redox Signaling* 29, 541-551.
52. Olguín-Albuerne, M., and Morán, J. (2017). Redox Signaling Mechanisms in Nervous System Development. *Antioxidants & Redox Signaling* 28, 1603-1625.
53. Oswald, M.C.W., Garnham, N., Sweeney, S.T., and Landgraf, M. (2018). Regulation of neuronal development and function by ROS. *FEBS letters* 592, 679-691.
54. Gauron, C., Meda, F., Dupont, E., Albadri, S., Quenech'Du, N., Ipendey, E., Volovitch, M., Del Bene, F., Joliot, A., Rampon, C., et al. (2016). Hydrogen peroxide (H<sub>2</sub>O<sub>2</sub>) controls axon pathfinding during zebrafish development. *Developmental biology* 414, 133-141.
55. Morinaka, A., Yamada, M., Itofusa, R., Funato, Y., Yoshimura, Y., Nakamura, F., Yoshimura, T., Kaibuchi, K., Goshima, Y., Hoshino, M., et al. (2011). Thioredoxin mediates oxidation-dependent phosphorylation of CRMP2 and growth cone collapse. *Sci Signal* 4, ra26.
56. Walker, A.K., Soo, K.Y., Levina, V., Talbo, G.H., and Atkin, J.D. (2013). N-linked glycosylation modulates dimerization of protein disulfide isomerase family A member 2 (PDIA2). *Febs j* 280, 233-243.
57. Solovyov, A., and Gilbert, H.F. (2004). Zinc-dependent dimerization of the folding catalyst, protein disulfide isomerase. *Protein science : a publication of the Protein Society* 13, 1902-1907.
58. Bastos-Aristizabal, S., Kozlov, G., and Gehring, K. (2014). Structural insight into the dimerization of human protein disulfide isomerase. *Protein science : a publication of the Protein Society* 23, 618-626.
59. Fu, X.M., and Zhu, B.T. (2009). Human pancreas-specific protein disulfide isomerase homolog (PDip) is an intracellular estrogen-binding protein that modulates estrogen levels and actions in target cells. *J Steroid Biochem Mol Biol* 115, 20-29.
60. Rainey-Barger, E.K., Mkrтчian, S., and Tsai, B. (2007). Dimerization of ERp29, a PDI-like protein, is essential for its diverse functions. *Mol Biol Cell* 18, 1253-1260.
61. Matsuo, Y., Masutani, H., Son, A., Kizaka-Kondoh, S., and Yodoi, J. (2009). Physical and functional interaction of transmembrane thioredoxin-related protein with major histocompatibility complex class I heavy chain: redox-based protein quality control and its potential relevance to immune responses. *Mol Biol Cell* 20, 4552-4562.
62. Hetz, C. (2012). The unfolded protein response: controlling cell fate decisions under ER stress and beyond. *Nat Rev Mol Cell Biol* 13, 89-102.

63. Barkovich, A.J., Guerrini, R., Kuzniecky, R.I., Jackson, G.D., and Dobyns, W.B. (2012). A developmental and genetic classification for malformations of cortical development: update 2012. *Brain* 135, 1348-1369.
64. Stutterd, C.A., and Leventer, R.J. (2014). Polymicrogyria: a common and heterogeneous malformation of cortical development. *Am J Med Genet C Semin Med Genet* 166c, 227-239.
65. Leventer, R.J., Jansen, A., Pilz, D.T., Stoodley, N., Marini, C., Dubeau, F., Malone, J., Mitchell, L.A., Mandelstam, S., Scheffer, I.E., et al. (2010). Clinical and imaging heterogeneity of polymicrogyria: a study of 328 patients. *Brain* 133, 1415-1427.
66. Brun, B.N., Mockler, S.R.H., Laubscher, K.M., Stephan, C.M., Wallace, A.M., Collison, J.A., Zimmerman, M.B., Dobyns, W.B., and Mathews, K.D. (2017). Comparison of brain MRI findings with language and motor function in the dystroglycanopathies. *Neurology* 88, 623-629.
67. Bahi-Buisson, N., Poirier, K., Boddaert, N., Fallet-Bianco, C., Specchio, N., Bertini, E., Caglayan, O., Lascelles, K., Elie, C., Rambaud, J., et al. (2010). GPR56-related bilateral frontoparietal polymicrogyria: further evidence for an overlap with the cobblestone complex. *Brain* 133, 3194-3209.
68. Jaglin, X.H., Poirier, K., Saillour, Y., Buhler, E., Tian, G., Bahi-Buisson, N., Fallet-Bianco, C., Phan-Dinh-Tuy, F., Kong, X.P., Bomont, P., et al. (2009). Mutations in the beta-tubulin gene TUBB2B result in asymmetrical polymicrogyria. *Nat Genet* 41, 746-752.
69. Barth, P.G. (1987). Disorders of Neuronal Migration. *Canadian Journal of Neurological Sciences / Journal Canadien des Sciences Neurologiques* 14, 1-16.
70. Liu, H.M., Bangaru, B.S., Kidd, J., and Boggs, J. (1976). Neuropathological considerations in cerebro-hepato-renal syndrome (Zellweger's syndrome). *Acta Neuropathol* 34, 115-123.
71. Melo, A.S.d.O., Aguiar, R.S., Amorim, M.M.R., Arruda, M.B., Melo, F.d.O., Ribeiro, S.T.C., Batista, A.G.M., Ferreira, T., dos Santos, M.P., Sampaio, V.V., et al. (2016). Congenital Zika Virus Infection: Beyond Neonatal Microcephaly. *Congenital Zika Virus Infection*. *JAMA Neurology* 73, 1407-1416.
72. Jansen, A.C., Robitaille, Y., Honavar, M., Mullatti, N., Leventer, R.J., Andermann, E., Andermann, F., and Squier, W. (2016). The histopathology of polymicrogyria: a series of 71 brain autopsy studies. *Developmental Medicine & Child Neurology* 58, 39-48.
73. Squier, W., and Jansen, A. (2014). Polymicrogyria: pathology, fetal origins and mechanisms. *Acta Neuropathol Commun* 2, 80.
74. Laguesse, S., Creppe, C., Nedialkova, D.D., Prevot, P.P., Borgs, L., Huysseune, S., Franco, B., Duysens, G., Krusy, N., Lee, G., et al. (2015). A Dynamic Unfolded Protein Response Contributes to the Control of Cortical Neurogenesis. *Dev Cell* 35, 553-567.
75. Deutsch, E.W., Csordas, A., Sun, Z., Jarnuczak, A., Perez-Riverol, Y., Ternent, T., Campbell, D.S., Bernal-Llinares, M., Okuda, S., Kawano, S., et al. (2017). The ProteomeXchange consortium in 2017: supporting the cultural change in proteomics public data deposition. *Nucleic Acids Res* 45, D1100-d1106.

76. Perez-Riverol, Y., Csordas, A., Bai, J., Bernal-Llinares, M., Hewapathirana, S., Kundu, D.J., Inuganti, A., Griss, J., Mayer, G., Eisenacher, M., et al. (2019). The PRIDE database and related tools and resources in 2019: improving support for quantification data. *Nucleic acids research* 47, D442-D450.

## FIGURE TITLES AND LEGENDS

**Figure 1. Features and brain MRI of individuals with *TMX2* variants.** P indicates the code of the probands as used in Table 1 and S4. P1 (**A-E**): affected member of family 1. **A**: The photograph shows mild microcephaly and no overt dysmorphic features. The MRI scan at birth shows T2 weighted images, of (**B**) parasagittal plane, (**C**) axial at the level of basal ganglia, (**D**) axial at the level of parietal areas and  $\epsilon$  axial at the level of pons and cerebellum. Both the parasagittal and the two axial cerebral sections show diffuse polymicrogyria of the cortex, normal myelination, hypointensity of the thalami (left axial) and normal cerebellum. P2 (**F-H**): MRI of the affected individual from family 2 at 19 months of age. (**F**) axial FLAIR -, (**G**) coronal T2 -, (**H**) coronal inversion recovery- weighted images all showing bilateral diffuse thickened cortex extending through frontal, parietal and occipital areas, resembling polymicrogyria, with sparing of the cerebellum. The lateral ventricles are enlarged and asymmetric; the periventricular white matter volume is strongly reduced. P3 (**I**): axial T2 weighted image of the affected child of family 3 at birth, showing diffuse bilateral polymicrogyria of the cortex, mild dilatation of the posterior horns of the lateral ventricles and delayed myelination. P4 (**J-L**) and P5 (**M-O**): affected siblings of family 4, at the age of 12 (P4) and 23 years (P5), respectively (**J and M**) sagittal T1-, (**K and N**) axial T2- weighted images at the level of basal ganglia and (**L and O**) the cerebellum, showing thin corpus callosum, loss of periventricular white matter and volume of thalami, deep cerebral sulci and mild cerebellar atrophy. No cortical malformation is present. P6 (**P-S**) is the index of family 5. (**P**) Axial T2 and (**Q**) parasagittal T1 images showing abnormally thick cortex, atrophic thalami, in (**Q**) the frontal cortex looks pachygyric. (**R**) Axial T2 FLAIR and (**S**) axial T1 weighted images showing diffusely thickened cortex, most prominent in parietal areas and moderately enlarged lateral ventricles. P9 (**T-V**): affected proband of family 6, at the age of 11 months. Axial T2 weighted images (**T-U**) showing brain atrophic changes with bilateral pallidus (red arrow) and posterior limb of the internal capsule (red arrowhead) T2 high signal intensity, as well as significant delayed myelination. Globi pallidi are severely atrophic. (**V**): Both globi pallidi, posterior limb of the internal capsules, optic radiations (black arrowhead) and brainstem tract (not shown) abnormalities are also noted on DWI and confirmed by ADC map (not shown) indicating restricted diffusion. P10 (**W-Y**): MRI at birth of the proband from family 7. (**W**) midsagittal, (**X-Y**) axial T2 weighted images. (**W**) mild hypoplasia of the pons, thin corpus callosum. (**X**) hypoplastic cerebral peduncles, bilateral abnormal cortex with polymicrogyric appearance. (**Y**) diffuse bilateral polymicrogyria, enlarged lateral ventricles with pseudocyst in the left occipital horn (black arrowhead), and white matter loss, the combination including the pseudocyst being typically seen in CMV infections.

**Figure 2. Brain pathology of individuals with *TMX2* variants.** A-C, E-G: affected individuals; D and H: age matched controls. Upper panel: macroscopic brain appearance of P1 (**A-B**) and P10 (**C**). Sagittal view (**A**) and coronal section (**B**) show diffuse bilateral excessive amount of small gyri (polymicrogyria) of the cerebral cortex (most affected areas indicated by white arrows), compared to control brain (**D**). (**C**) coronal section through the posterior parts of the brain shows asymmetric

hemispheres and bilateral polymicrogyria, especially in the occipital lobes (white arrow). The image of the normal neonatal age-matched brain (40GW), shows normal size and number of the gyri and sulci (lateral view of the right hemisphere) (**D**). Lower panel: Histological sections of individuals P1 (**E-F**), P10 (**G**) and age matched control brain cortex (**H**) show absence of normal cortical layers in affected individuals, with bands of neurons laying perpendicular to the cortical surface in E, F and G. Undulating bands of neurons (arrow heads), entrapped pial vessels mimicking fusion of the cortical layer (arrow), and thickened leptomeninges are compatible with (unlayered) polymicrogyria (**E**: H&E, 10x, **F**: H&E, 5x, **G**: Lugol-PAS stain, 3x). Control histological section of the frontal dorsolateral telencephalic gyrus of the neonatal age-matched brain (**H**: H&E 5x), showed the regular organization of the six-layered neonatal neocortex, parallel to the pia surface.

**Figure 3. Genomic and transcriptomic analysis of *TMX2* variants.** **A.** Schematic overview of *TMX2*, protein domains and the discovered variants in affected individuals (GSDS 2.0) **B.** Levels of expressed *TMX2* messenger RNA in individuals P1, P2 and P3. Ct values were normalized with two housekeeping genes *CLK2* and *RNF111*( $\Delta\Delta$  CT relative to control (n=2). Data are represented as the mean  $\pm$  SEM. Statistical two-tailed unpaired t-tests were performed with confidence interval 95%. **C.** Allele specific qPCR of individual P1. Ct values were normalized with two housekeeping genes *CLK2* and *RNF111* ( $\Delta\Delta$  CT relative to control (n=4). **D.** Aberrant splicing of the P2 and control *TMX2* alleles. Graphic illustration (adapted from IGV Sashimi plot) of the percentage of *TMX2* transcripts in RNAseq data of total RNA of individual P2 and 1 control individual. Percentages are calculated for each transcript compared to the total *TMX2* (wild-type and alternative) transcript reads (GRCh38), and **E.** Aberrant splicing of the P2 and control *TMX2* alleles. Aligned uniquely mapped reads in the exon 5-7 region of *TMX2* were quantified (reads per million) using IGV 2.3.26. Three distinct alternative species of *TMX2* transcript were identified, consistent with intron 6 retention, exon 6 skipping and exon 6 internal splice site usages, the latter two only from the P2 allele. Total uniquely mapped reads for control and individual P2 were 64 745 034 and 54 200 090 respectively.

**Figure 4. Gene ontology (GO) analysis of differentially expressed genes in *TMX2* variants.** **A.** DAVID Functional Annotation Clustering (FAC) analysis of the top 1000 differentially expressed genes (DEGs) obtained by comparison of two *TMX2* affected individuals vs. three age and gender matched control RNA samples (p-value <0.05). **B.** upper panel: LogFC of all differentially expressed disulfide bond associated genes in *TMX2* affected individuals with an FDR<0.05, lower panel: -Log(FDR) of these genes (-log(FDR)<1.3). **C.** Ingenuity Pathway analysis (IPA) was performed to determine activated and inhibited biological functions downstream of the differentially expressed genes in *TMX2* affected individuals. Stringency was determined with 90% confidence interval by only considering activation Z-scores higher than 1.65 (activation) or lower than -1.65 (inhibition). Individual p-values of each function are mentioned within the bars and were always lower than  $10^{-6}$ . **Abbreviations:** GO, Gene ontology; UP, UniProtKB; FDR, False discovery rate; FC, Fold Change; KEGG, Kyoto Encyclopedia of Genes and Genomes.

**Figure 5. Proteomics analysis of exogenous *TMX2* interacting proteins.** **A.** HEK293T cells were transfected with Myc-tagged *TMX2* or negative control  $\beta$ -lactamase for 24 hours, followed by IP with  $\alpha$ Myc antibody and LC-MS/MS on bead pellets. Detected proteins interacting with *TMX2*-Myc but not with Lac-Myc were filtered based on average Mascot score in n=4 experiments (significant if higher than 40). Cytoscape String App visualized all 71 proteins reproducibly and selectively

interacting with TMX2 according to pathway involvement (dark blue=Protein folding, light blue= Calcium Homeostasis, Red= ER associated degradation (ERAD) and Unfolded Protein Response (UPR), Green= Mitochondrial signaling, Pink= Mitosis, Orange= Translation, Yellow= Nucleus Transport, Black=Golgi transport, Grey=unassigned). Known PDI interactors Calnexin and SERCA2 were found in the top 10 highest interactions, and are circled in red. **B.** HEK293T cells were transfected with Myc-tagged TMX2 or negative control  $\beta$ -lactamase for 24 hours, followed by reciprocal immunoprecipitation of SERCA2 (Mouse monoclonal anti-SERCA2 ATPase ab2861) and Calnexin (Monoclonal Rabbit anti-human CNX C5C9), SDS PAGE and detection of TMX2 with  $\alpha$ Myc antibody. IP input is shown after reducing western blot.

**Figure 6. Bioenergetics profiles of skin fibroblasts from affected individuals with *TMX2* variants. A, B.** Oxygen consumption rate (OCR) and extracellular acidification rate (ECAR) bioenergetics profiles of fibroblasts derived from healthy controls (n=4) and affected individuals (P1, P2, P3). Fibroblasts were challenged with sequential administration of oligomycin to inhibit ATP synthase, FCCP to elicit maximal respiration, rotenone to inhibit complex I, and antimycin to inhibit complex III and fully block respiration. The parameters analyzed in the profiles were: basal respiration, respiration dedicated to ATP production, (measured as difference between basal respiration and the respiration after oligomycin injection), mitochondrial reserve capacity (as difference between maximum reserve capacity and basal respiration), and rotenone sensitive respiration (which accounts for the respiration dependent on complex I), basal glycolysis and oligomycin stimulated glycolysis. **C, D.** Fibroblasts derived from affected individuals show significant reduction in mitochondrial reserve capacity and in the complex I activity (**C**) while showing a significant potentiation of glycolysis in basal condition and upon stimulation with oligomycin (**D**). **E.** The analysis of mitochondrial respiration in galactose medium (where glycolysis is not permitted) highlights the inability of the *TMX2* variant fibroblasts to potentiate basal mitochondrial respiration and mitochondrial complex I activity. (\*p < 0.05; \*\*p < 0.01; \*\*\*\*p < 0.0001; one-way ANOVA (C, D) and two-way ANOVA (E) followed by Dunnett's multiple-comparison post doc test). Graphs represent mean  $\pm$  SEM.

**Figure 7. Redox state assays of wild-type and variant *TMX2*. A-B.** Non-reducing western blot of exogenous wild-type *TMX2* versus endogenous control PDI (PDIA1) in HEK293T cells, showing that *TMX2* occurs in an oxidized and reduced monomeric form, while during H<sub>2</sub>O<sub>2</sub> treatment a dimer is formed (OX dimer). A) left panel shows the blot after incubation with anti-wild-type *TMX2* antibodies; middle panel: incubation with anti-Myc antibodies; right panel: anti-PDI control protein antibodies. B) Control experiment after expression of exogenous control  $\beta$ -lactamase (Lac-Myc); immunoblotting performed with the same antibodies as in A. Native: untreated cells; BFA: cells treated with ER stress inducer Brefeldin A; DTT: cells treated with reducing agent DL-Dithiothreitol; H<sub>2</sub>O<sub>2</sub>: cells treated with hydrogen peroxide.

**C.** Non-reducing western blot with similar experimental setup as in A and B. but here also after addition of ER stress inducers Tunicamycin (TM) and Thapsigargin (TG). Redox states of TRX domain p.Cys170Gly variant (lanes 7-12) and affected individual p.Arg53Cys variant (lanes 13-18) and p.Arg231Trp variant (lanes 19-24) were determined simultaneously. Detection was performed with anti-Myc antibody. **D-E.** Semi quantitative densitometry calculations of *TMX2* dimer/monomer ratios in native, ER stress, oxidative and reductive environment for wild-type *TMX2*, n=4 western blots from biological replicates (**D**.) and comparing wild-type *TMX2* to p.Cys170Gly, p.Arg53Cys and p.Arg231Trp variants. Data are represented as the mean  $\pm$  SEM. Statistical two-tailed unpaired t-

tests were performed with confidence interval 95% in Graphpad Prism 8 (\*p < 0.05; \*\*p < 0.01; \*\*\*p<0.001, \*\*\*\*p < 0.0001).

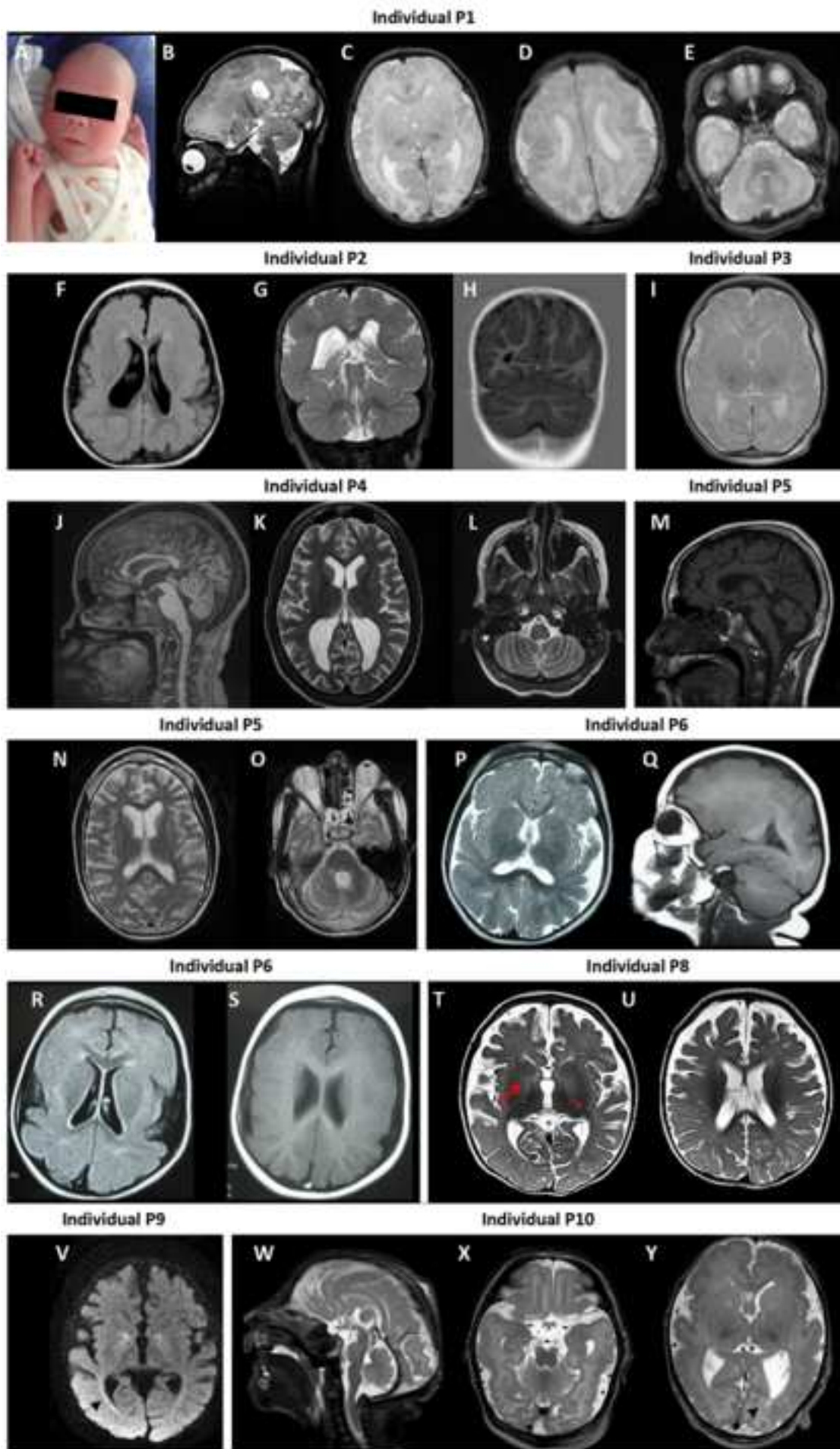
## TABLE TITLES AND LEGENDS

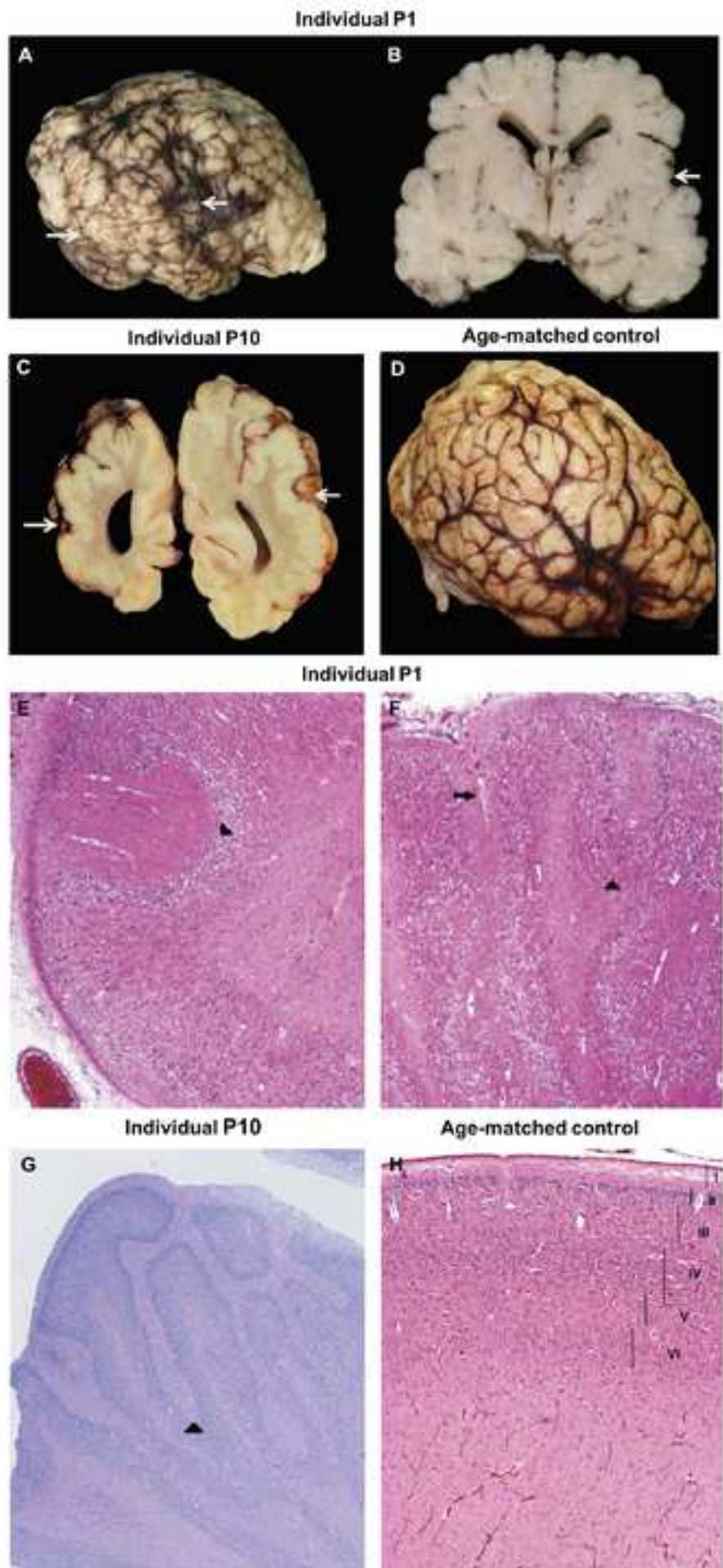
**Table 1** Summary of *TMX2* variants and phenotypes.

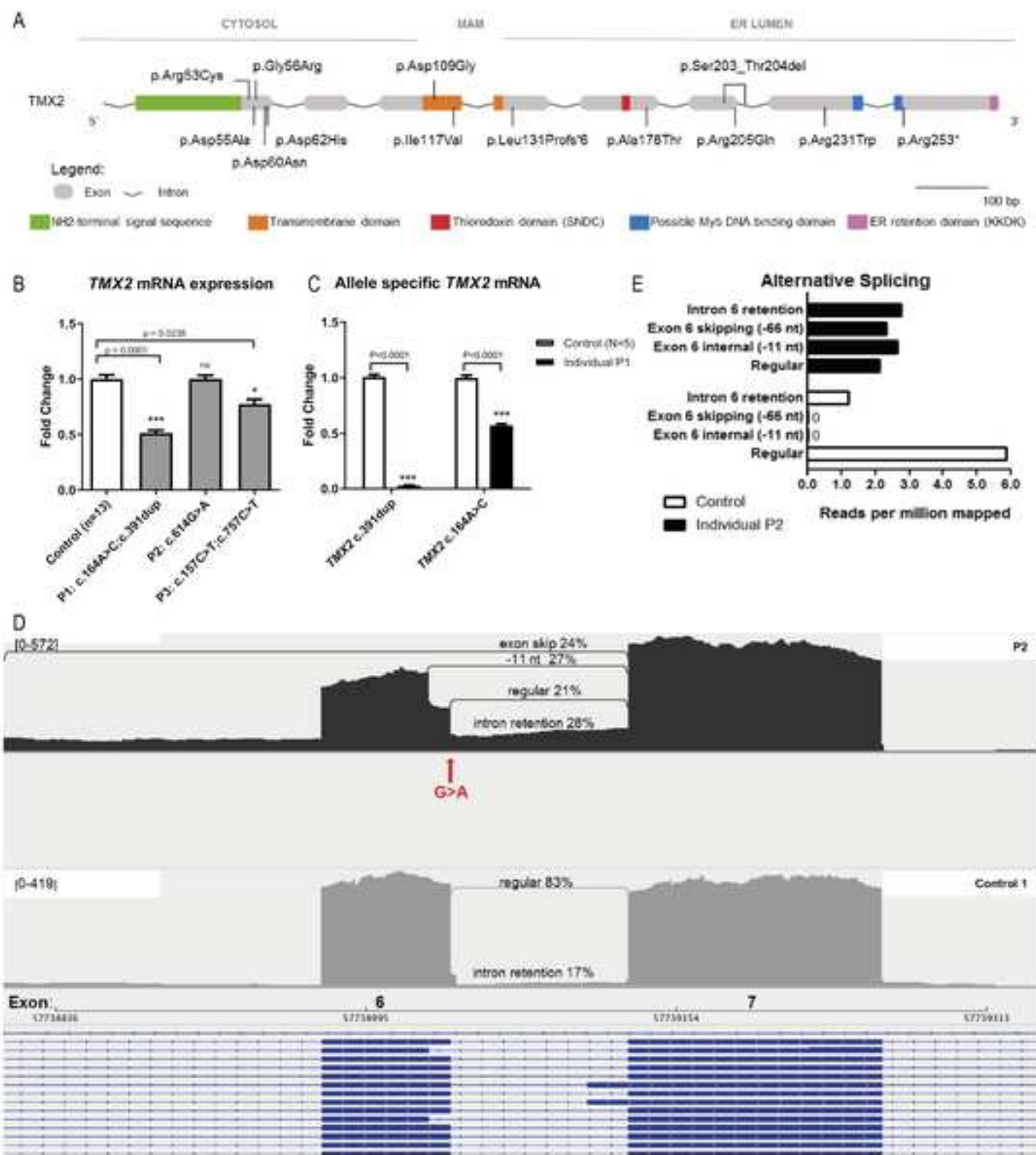
Affected individuals	Family 1- P1	Family 2- P2	Family 3-P3	Family 4- P4	Family 4- P5	Family 5-P6 <sup>24</sup>	Family 5-P7 <sup>24</sup>	Family 6- P8	Family 6- P9	Family 7- P10	Family 8- P11	Family 8- P12	Family 9- P13	Family 10- P14
<b>Ancestry</b>	Dutch	Portuguese	White British	Puerto Rican	Puerto Rican	Spanish	Spanish	Arab	Arab	Dutch	Iraqi	Iraqi	Pakistani	Mexican
<b>cDNA alteration</b>	c.164A>C; c.391dup	c.614G>A Homozygote	c.157C>T; c.757C>T	c.166G>C Homozygote	c.166G>C Homozygote	c.326A>G; c.691C>T	c.326A>G; c.691C>T	Not tested	c.532G>A Homozygote	c.164A>C;c.609 _614+15del	c.184G>C Homozygote	c.184G>C Homozygote	c.178G>A Homozygote	c.349A>G; c.691C>T
<b>Protein alteration</b>	p.Asp55Ala;p.Leu131Profs*6	p.Arg205Gln	p.Arg53Cys;p.Arg253*	p.Gly56Arg	p.Gly56Arg	p.Asp109Gly;p.Arg231Trp	p.Asp109Gly;p.Arg231Trp	Not tested	p.Ala178Thr	p.Asp55Ala;p.Ser203_Thr204del	p.Asp62His	p.Asp62His	p.Asp60Asn	p.Ile117Val;p.Arg231Trp
<b>Gender</b>	Male	Male	Female	Male	Female	Female	Male	Female	Female	Male	Male	Male	Female	Female
<b>Head size (OFC)</b>	Primary microcephaly (- 3 SD at birth)	Microcephaly (n.a. at birth; - 4.5 SD current)	Primary microcephaly (- 2.5 SD at birth; - 6.7 SD current)	Borderline microcephaly (n.a. at birth; - 2 SD current)	Microcephaly (n.a. at birth; - 3 SD current)	Microcephaly (- 2 SD at birth; - 4 SD current)	Microcephaly (n.a. at birth; - 3 SD current)	Undefined (0 SD at birth, later n.a. )	Microcephaly (0 SD at birth; - 5.5 SD current)	Primary microcephaly (- 2.5 SD at birth)	Microcephaly (n.a. at birth; - 4.5 SD current)	Primary microcephaly (- 2.5 SD at birth; - 3.5 SD current)	Normal (n.a. at birth; - 0.5 SD current)	Normal (n.a. at birth; - 0.8 SD current)
<b>Neurological impairment</b>	No developmental milestones <sup>a</sup>	CP, no speech or ambulation	CP, no speech or ambulation	CP, no speech or ambulation	CP, no speech or ambulation	CP, no speech or ambulation	CP, no speech or ambulation	CP, no speech or ambulation	CP, no speech or ambulation	No developmental milestones <sup>a</sup>	No ambulation, few words	No speech or ambulation	Able to walk with support, few words	IQ 62; language disorder; hyperactive behavior, able to walk
<b>Survival/ age at last examination</b>	Deceased at week 2	7 yr.	9 yr.	28 yr.	25 yr.	13 yr.	11 yr.	Deceased at 6 yr.	1.5 yr.	Deceased at 1 week	10 yr.	5 yr.	4.8 yr.	11.5 yr.
<b>Epilepsy</b>	Generalized, apnea, status epilepticus	Generalized, absence, spasms	Generalized seizures	Focal seizures	Myoclonic-absence, GTC	No seizures	GTC	GTC	Focal seizures	Apnea, diaphragmatic myoclonia	Generalized tonic, myoclonic seizures	GTC	Myoclonic status epilepticus	No seizures
<b>MRI</b>	Polymicrogyria	Polymicrogyria	Polymicrogyria	Progressive brain atrophy	Progressive brain atrophy	Pachygyria	Pachygyria	Severe brain atrophy	Severe brain atrophy	Polymicrogyria	n.a.	Polymicrogyria	Hemihypertrophy and frontal dysgyria	Normal
<b>Brain autopsy</b>	Unlayered polymicrogyria and complete cortical disorganization	n.a.	n.a.	n.a.	n.a.	n.a.	n.a.	n.a.	n.a.	Diffuse polymicrogyria and cobblestone-like malformation	n.a.	n.a.	n.a.	n.a.

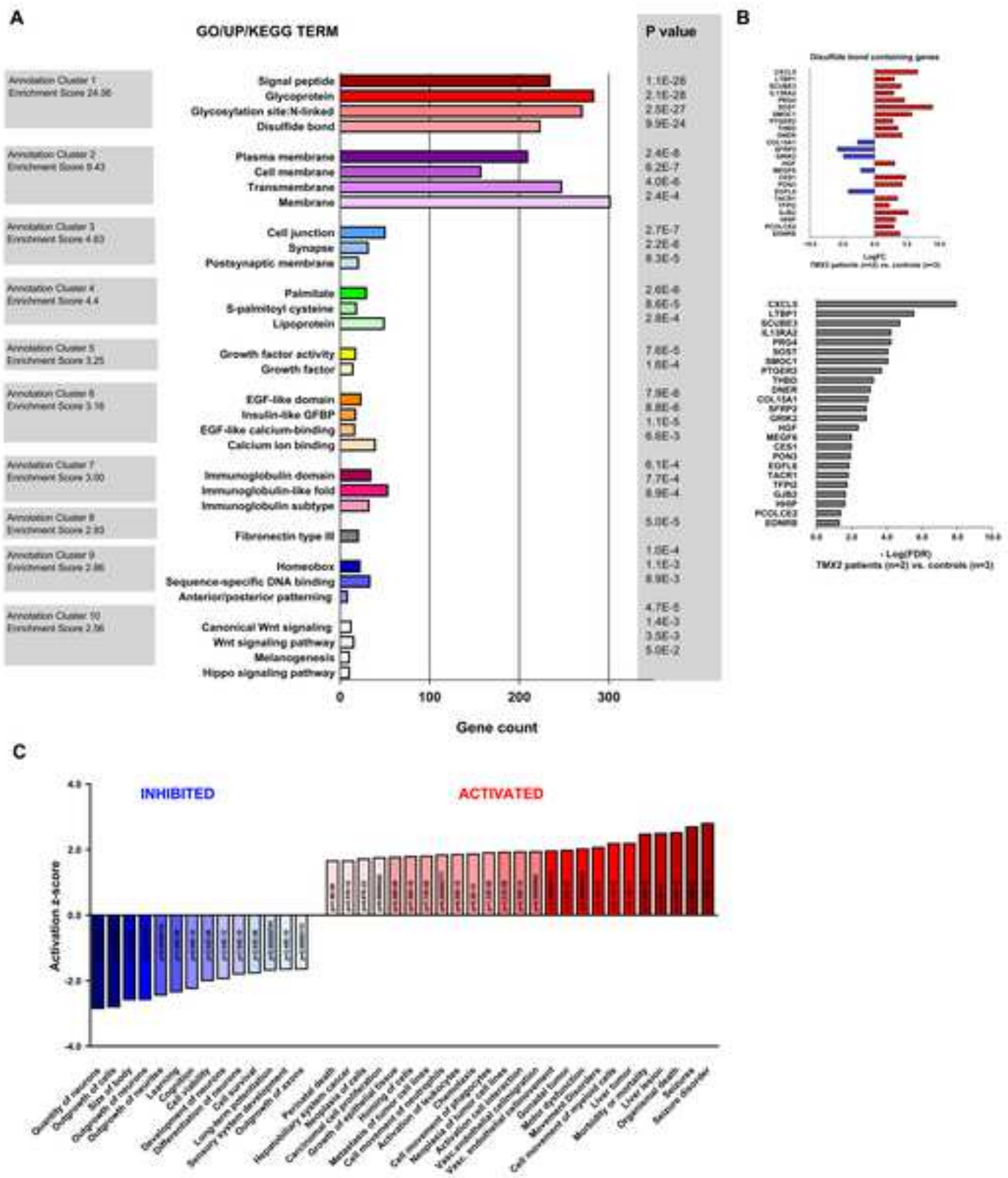
<sup>a</sup> These individuals passed away soon after birth. Microcephaly is defined as an OFC  $\leq$ -2.5SD. Abbreviations: CP, signs of cerebral palsy; n.a., not assessed or not available; OFC, Occipitofrontal circumference; yr., year; SD, standard deviations; GTC, Generalized tonic clonic seizures



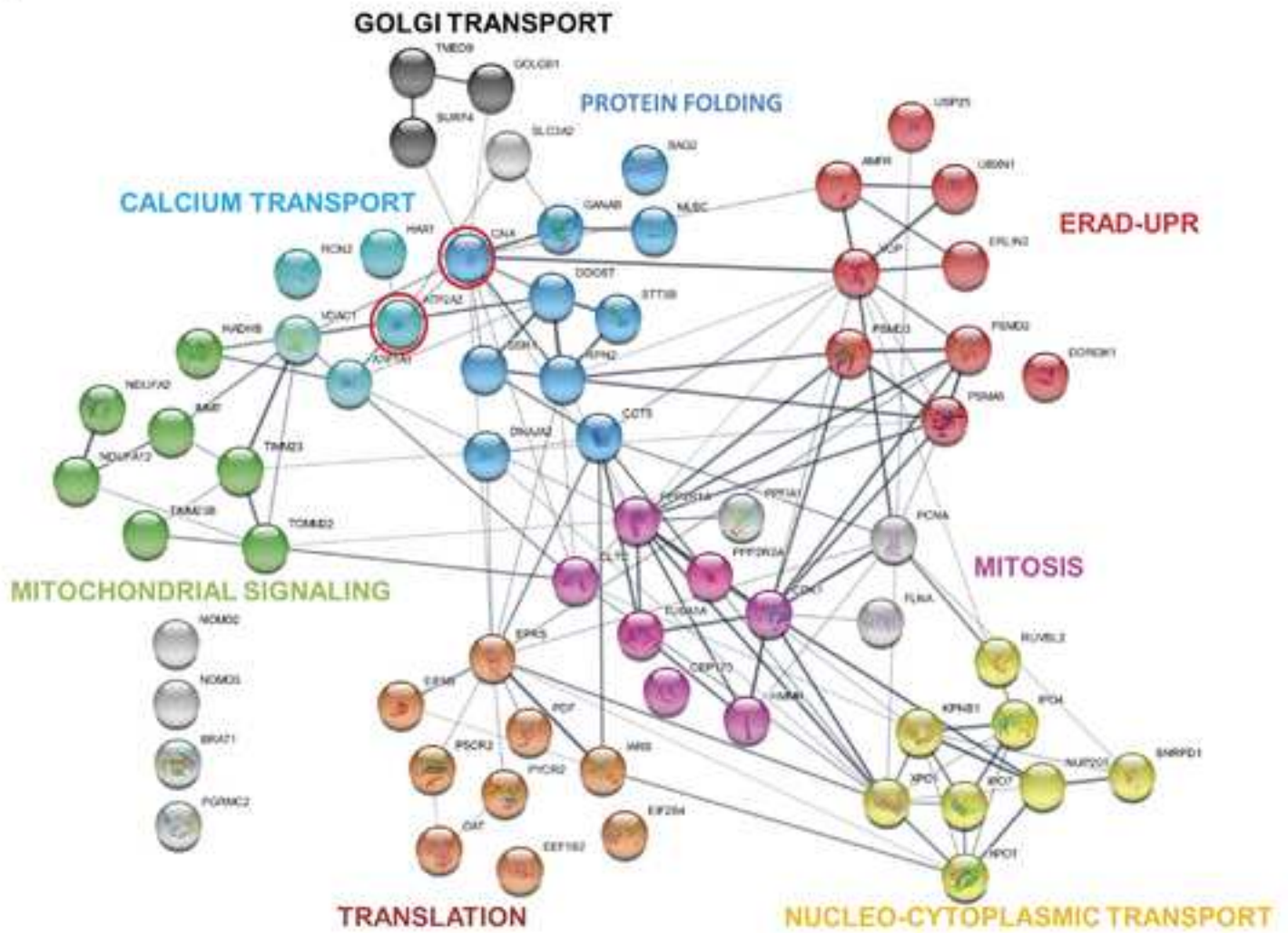




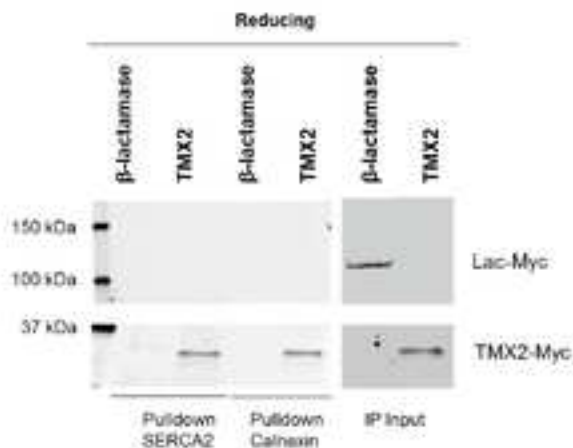


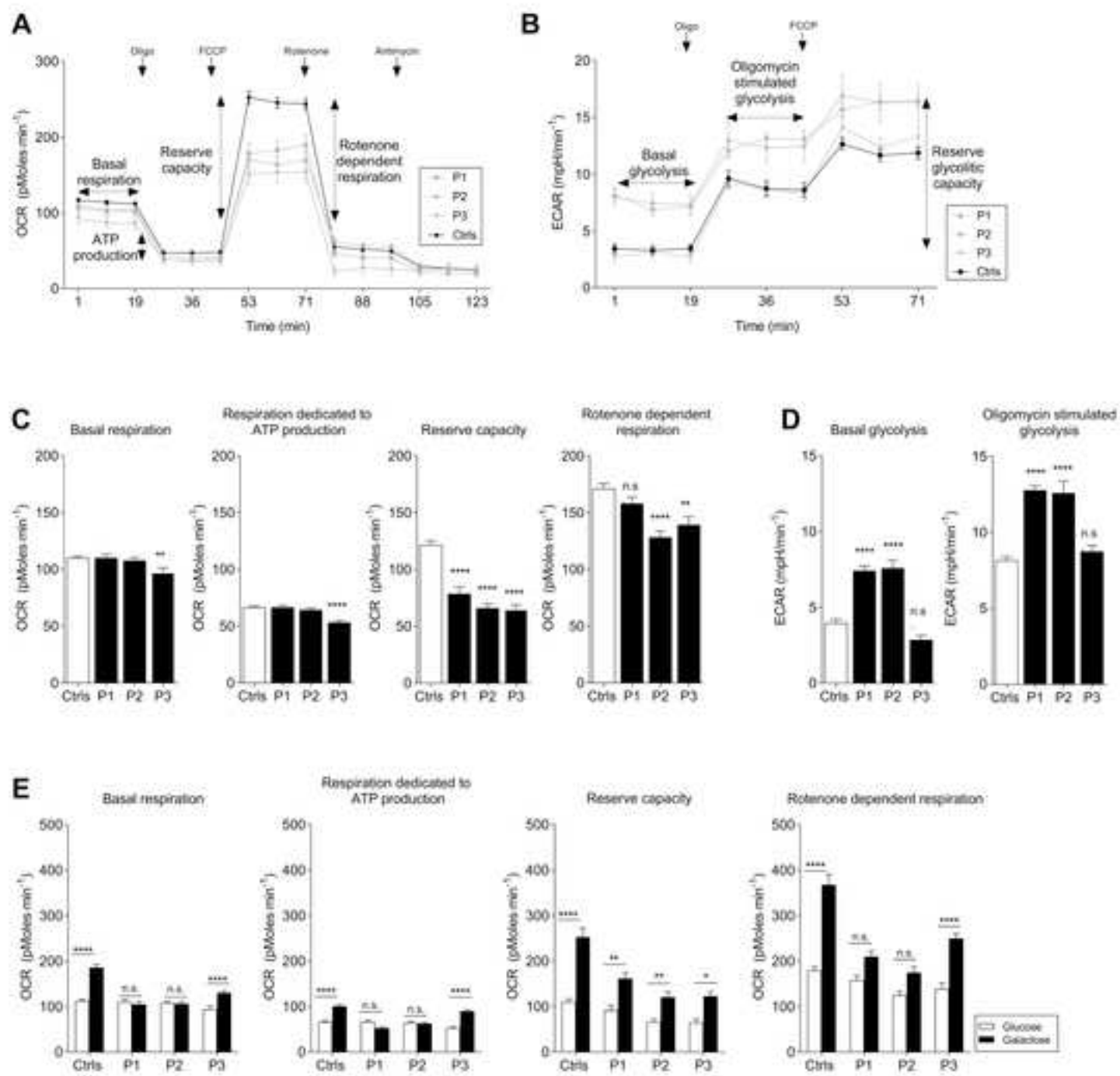


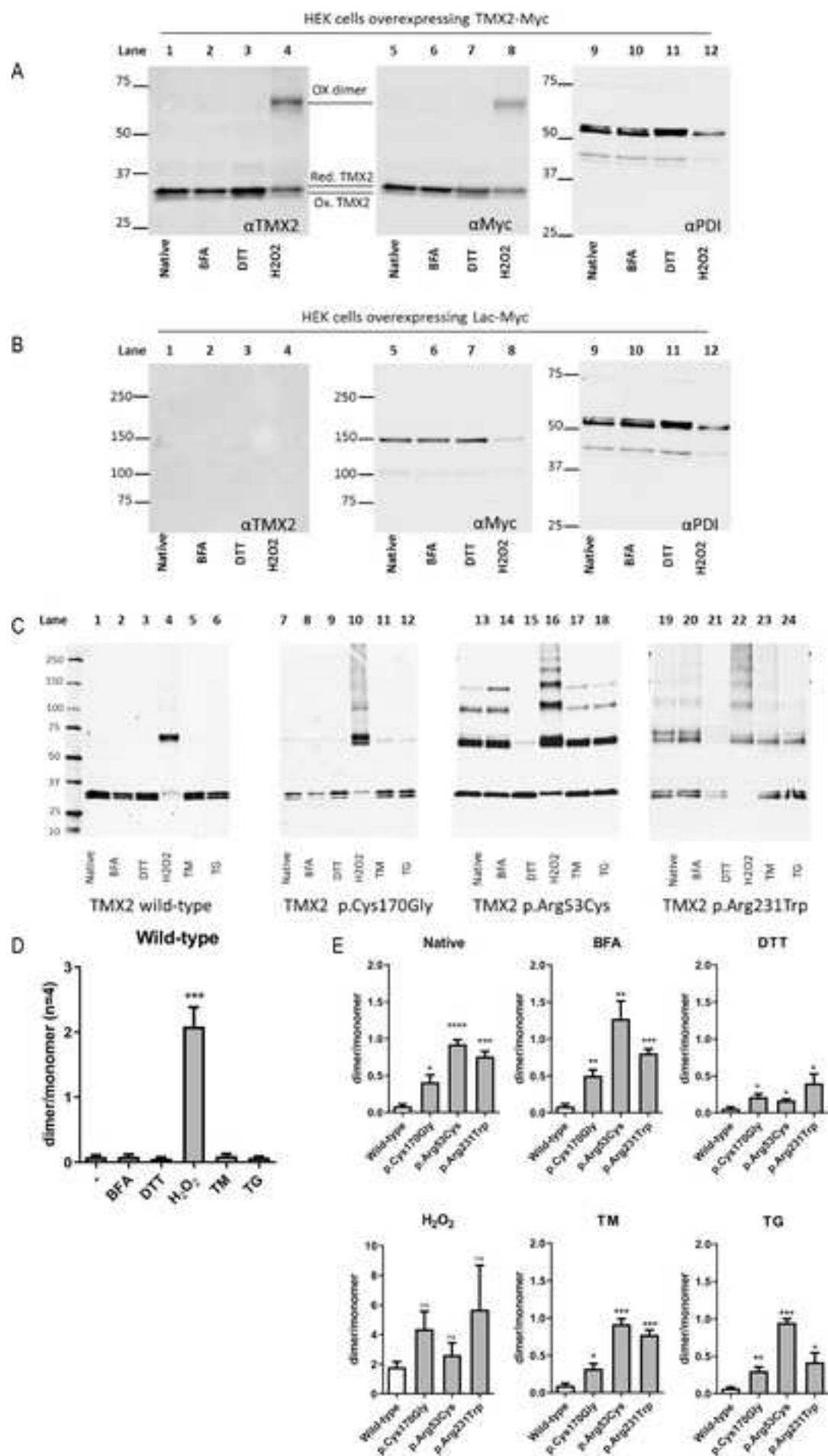
A

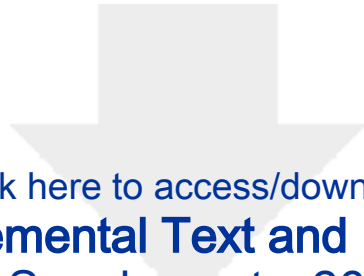


B



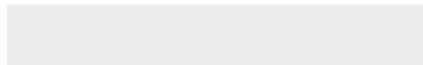






[Click here to access/download](#)

**Supplemental Text and Figures**  
R3 TMX2 Supplements\_26-09-19.pdf



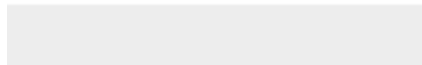




[Click here to access/download](#)

**Supplemental Movies and Spreadsheets**

Table S5 Proteomics.xlsx





[Click here to access/download](#)

**Supplemental Movies and Spreadsheets**  
Table S4\_Clinic\_official\_170919.xlsx

